Journal of Hazardous Materials 452 (2023) 131249

Contents lists available at ScienceDirect

Journal of Hazardous Materials

journal homepage: www.elsevier.com/locate/jhazmat

Research Article

Interface engineering of Mn_3O_4/Co_3O_4 S-scheme heterojunctions to enhance the photothermal catalytic degradation of toluene

Jungang Zhao [a,b], Caiting Li [a,b,*], Qi Yu [a,b], Youcai Zhu [a,b], Xuan Liu [a,b], Shanhong Li [a,b], Caixia Liang [a,b], Ying Zhang [a,b], Le Huang [a,b], Kuang Yang [a,b], Ziang Zhang [a,b], Yunbo Zhai [a,b]

[a] *College of Environmental Science and Engineering, Hunan University, Changsha 410082, PR China*
[b] *Key Laboratory of Environmental Biology and Pollution Control, Hunan University, Ministry of Education, Changsha 410082, PR China*

HIGHLIGHTS

- Mn_3O_4/Co_3O_4 exhibit superior photothermal catalytic activity than Mn_3O_4 and Co_3O_4, respectively.
- The composite of Mn_3O_4/Co_3O_4 forms an S-type heterojunction.
- Mn_3O_4/Co_3O_4 couples the thermal and photoelectric effects of UV–vis light.
- Photothermal conversion pathways of toluene on Mn_3O_4/Co_3O_4 were investigated.
- This work offers a new idea for the fabrication of photothermal catalysts.

GRAPHICAL ABSTRACT

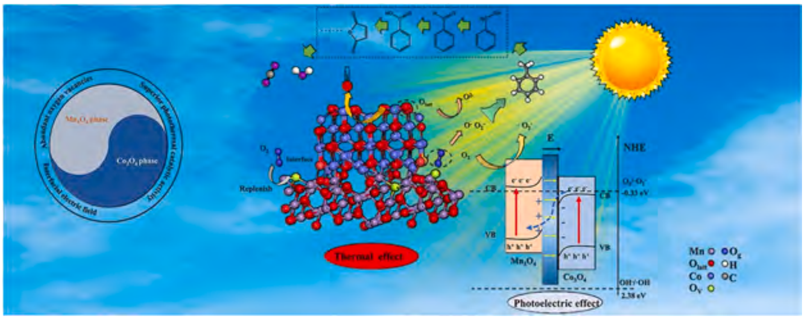

ARTICLE INFO

Editor: Zaher Hashisho

Keywords:
Photothermal catalysis
S-scheme heterojunction
Toluene
Interfacial effect
DFT calculations

ABSTRACT

Transition metal oxides have high photothermal conversion capacity and excellent thermal catalytic activity, and their photothermal catalytic ability can be further improved by reasonably inducing the photoelectric effect of semiconductors. Herein, Mn_3O_4/Co_3O_4 composites with S-scheme heterojunctions were fabricated for photothermal catalytic degradation of toluene under ultraviolet-visible (UV-Vis) light irradiation. The distinct heterointerface of Mn_3O_4/Co_3O_4 effectively increases the specific surface area and promotes the formation of oxygen vacancies, thus facilitating the generation of reactive oxygen species and migration of surface lattice oxygen. Theoretical calculations and photoelectrochemical characterization demonstrate the existence of a built-in electric field and energy band bending at the interface of Mn_3O_4/Co_3O_4, which optimizes the photogenerated carriers' transfer path and retains a higher redox potential. Under UV-Vis light irradiation, the rapid transfer of electrons between interfaces promotes the generation of more reactive radicals, and the Mn_3O_4/Co_3O_4 shows a substantial improvement in the removal efficiency of toluene (74.7%) compared to single metal oxides (53.3% and 47.5%). Moreover, the possible photothermal catalytic reaction pathways of toluene over Mn_3O_4/Co_3O_4 were also investigated by in situ DRIFTS. The present work offers valuable guidance toward the design and fabrication of efficient narrow-band semiconductor heterojunction photothermal catalysts and provides deeper insights into the mechanism of photothermal catalytic degradation of toluene.

---

* Corresponding author at: College of Environmental Science and Engineering, Hunan University, Changsha 410082, PR China.
E-mail address: ctli@hnu.edu.cn (C. Li).

https://doi.org/10.1016/j.jhazmat.2023.131249
Received 22 November 2022; Received in revised form 10 March 2023; Accepted 19 March 2023

1. Introduction

The growth in fossil fuel consumption [80,79], and the development of petrochemical and chemical industries, coupled with the use of a large number of paints, has led to a yearly increase in volatile organic compounds (VOCs) emissions [16,54,91]. As a common precursor of ozone and $PM_{2.5}$, the removal of VOCs has become an essential challenge for atmospheric environmental management [17,28]. Various technologies have been developed for the end-of-pipe treatment of VOCs, including adsorption [44,85], catalytic combustion [45,72], and plasma [32,90]. However, the strategy of adsorption is to immobilize VOCs into adsorbent to prevent fugitive dispersion, but cannot achieve the decomposition of pollutants, while catalytic combustion and plasma technologies often require the loading of precious metals and consume large amounts of energy to meet the intensity of thermal or electric fields required for pollutant decomposition. In the background of the global efforts to reduce carbon emissions, it is extremely necessary to explore an efficient, low-energy, and environmental-friendly treatment technology.

Photothermal catalysis is an emerging green catalytic technology in recent years, which is widely studied in the fields of VOCs removal [25,58], CO_2 reduction [30,48], hydrogen evolution [60,62], and methane reforming [36,82]. Different from conventional photocatalysis [13,38,56,76], photothermal catalysis also utilizes the light-driven thermal effect to raise the surface temperature of catalysts, thus it is possible to realize the coupling of the thermal and photoelectric effects to bring about higher catalytic efficiency [13,40,56]. Generally, there are two main strategies to design and fabricate photothermal catalysts for VOCs removal: (a) combining thermally active narrow bandgap metal oxides (MnO_x, CoO_x, CuO_x, FeO_x) with photothermal materials (graphene, carbon nanotube, MXene) or precious metal particles (Au, Pt, Ag) to improve light absorption and photothermal conversion to achieve higher surface temperatures for catalytic combustion of VOCs [27,37,75]; (b) construction of composite catalysts with narrow bandgap and wide bandgap semiconductors to achieve photothermal catalytic degradation of VOCs by using the synergistic effects between photoelectric effect induced by low wavelength sunlight (UV) and thermal effect induced by the medium and long wavelength sunlight (visible or infrared light), such as TiO_2/CuO [41], TiO_2/Co_3O_4 [67], $C/MnO/TiO_2$ [59], and $ZnO/La_{0.8}Sr_{0.2}CoO_3$ [64]. Nevertheless, few studies have been conducted to improve the photothermal catalytic properties of narrow bandgap semiconductors composite catalysts by exploiting their photoelectric effects. This may be because the conduction band (CB) and valence band (VB) potential of narrow bandgap semiconductors generally cannot reach the potential of $O_2/\cdot O_2^-$ and $H_2O/\cdot OH^-$ to generate active radicals, and their photogenerated carriers compounding rate is fast. However, if the overall energy band width of the composite is expanded by the construction of Z- or S-type heterostructures while retaining the broad spectral absorption capability of the respective narrow-band semiconductors [3,4,2,25], it is expected to become an ideal photothermal catalyst for VOCs degradation.

Manganese and cobalt-based oxides are among the most studied materials for thermocatalytic oxidation of VOCs due to their multiple valence states, high oxygen storage capacity, high abundance on earth, and cheap price [10,61,77,84]. Moreover, given their narrow bandgap, dark appearance, and excellent light absorption and photothermal conversion properties, they have also been extensively studied in photothermal catalysis in recent years [24,66,74]. While the research of manganese-cobalt mixed oxides in the field of photothermal catalysis is still relatively little reported. There is also a lack of in-depth understanding of the relationship between the interfacial characteristics, energy band structure, and photothermal catalytic performance of manganese and cobalt oxides heterojunction.

In this work, by rational fabricating narrow bandgap oxide heterojunction, the photothermal degradation of toluene over manganese-cobalt composite oxide was investigated under continuous flow conditions. The Mn_3O_4/Co_3O_4 heterojunction composite with distinct phase interfaces exhibited better photothermal catalytic activity compared to monometallic oxides. Experimental characterization and theoretical calculations demonstrated that the abundant heterogeneous interface favored the generation of oxygen defects, improved the migration of surface lattice oxygen, and accelerated oxygen recycling by adsorption of activated oxygen molecules at the interface. Moreover, the difference in energy band and work function enabled Mn_3O_4/Co_3O_4 to form an S-scheme heterojunction, which was conducive to retaining a higher redox potential, accelerating electron transfer, and producing more reactive oxygen species under light irradiation. Meanwhile, the photothermal oxidation pathways of toluene were investigated by in situ DRIFTS. Furthermore, the Mn_3O_4/Co_3O_4 demonstrated superior stability, water resistance, and operational flexibility.

2. Materials and methods

2.1. Materials and chemicals

The reagents manganese acetate, cobalt nitrate, ammonia (25–28 vol %), and ethanol (99%) were obtained from Sinopharm Chemical Reagent Co, Ltd. All the reagents are of analytical purity and do not require further purification for use. The gases of O_2 and N_2 were of high purity (99.999%) and purchased from Changsha Rizhen Gas Co., Ltd.

2.2. Catalysts preparation

Preparation of Mn-Co composite oxides: Mn-Co composite oxides were synthesized by the hydrothermal coprecipitation method. Firstly, a certain mass of $Mn(CH_3COO)_2\cdot 4\ H_2O$ and $Co(NO_3)_2\cdot 6\ H_2O$ were dissolved in 70 mL of deionized water and stirred for 30 min to form a transparent solution. Wherein, the total amount of Mn and Co was 10 mmol, and the molar ratio of Mn: Co was 1:9, 3:7, 5:5, 7:3, and 9:1, respectively. Subsequently, 15 mL ammonia was added dropwise into the mixture solution and stirred for 1.5 h. The suspension was then transferred to a 100 mL Teflon-lined autoclave and maintained at 160 °C for 12 h. When the reaction was finished, the autoclave was cooled naturally to room temperature. Consequently, the sediment was washed three times successively with deionized water and ethanol and dried at 70 ℃ overnight. Finally, the metal oxide precursors were calcined at 500 ℃ for 2 h with a ramp of 2 ℃/min to get the final catalysts, which were named Mn_xCo_{10-x} ($x = 1,3,5,7,9$). The process of synthesizing Mn_3O_4 and Co_3O_4 is similar to the above, with the difference that only $Mn(CH_3COO)_2\cdot 4\ H_2O$ or $Co(NO_3)_2\cdot 6\ H_2O$ was used. Mn_3O_4/Co_3O_4 in the following is another name for Mn_5Co_5 sample.

2.3. Material characterization

X-ray diffraction (XRD) of catalysts was carried out on a Rigaku SmartLab power diffractometer (Cu Kα radiation) with a scan rate of 5°/min. X-ray photoelectron spectroscopy (XPS, Thermo Scientific) was employed to analyze the valence state and electron transfer of catalysts. The nitrogen adsorption and desorption curves of the catalysts were recorded by Quantachrome Nova 4000e. And the specific surface area (S_{BET}) and pore volume (Vp) were calculated by the Brunauer-Emmett-Teller (BET) and Barret-Joyner-Halenda (BJH) methods. Raman spectrum was performed on a HOBIBA spectrometer with an excitation wavelength of 532 nm. The morphology and structure of the prepared samples were characterized using a scanning electron microscope (SEM, TESCAN MIRA4) and transmission electron microscope (TEM, FEI Tecnai G2 F20). Electron paramagnetic resonance (EPR, Bruker EMXplus-6/1) spectra were carried out to detect the oxygen vacancy. Ultraviolet-visible (UV-Vis, PerkinElmer Lambda750S) spectroscopy was performed at room temperature to test the light absorption capacity of the as-prepared samples. H_2 temperature-programmed reduction (H_2-TPR) was performed on a Micromeritics AutoChem II 2920 adsorption instrument. Before the test, the samples (50 mg) were pretreated in He flow (50 mL/min) at 300 °C for 60 min to remove the absorbed water and impurities species. After natural cooling to room temperature, the thermal conductivity detector (TCD) signal was recorded as the temperature raised at a ramp of 10 °C/min up to 800 °C in 5% H_2/Ar stream (50 mL/min). Similarly, the O_2 temperature-programmed desorption (O_2-TPD) was conducted on the same apparatus. In brief, 80 mg catalyst was pretreated in 10% O_2/He flow (50 mL/min) at 200 °C for 1 h and cooled to ambient temperature. Then the prepared samples were heated in He gas stream (50 mL/min) from 50° to 800°C at a rate of 10 °C/min. To study the adsorption and desorption ability of samples for toluene, the toluene temperature-programmed desorption tests (toluene-TPD) were employed on equipment built by our laboratory. The 100 mg sample was pretreated with 50 mL/min N_2 flow at 500 °C for 1 h, then cooled to 30 ℃. The samples were exposed to 500 ppm toluene/N_2 with a flow rate of 50 mL/min to saturation, after which the sample was purged with N_2 for 3 h to remove weakly adsorbed toluene. The temperature was then ramped up to 500 °C at a rate of 1 °C/min while toluene desorption data were recorded with the FID detector. The electrochemical measurements of the transient photocurrent, electrochemical impedance spectroscopy (EIS), and Mott-Schottky were performed in a standard three-electrode cell connected to an electrochemical workstation (CHI760E). The electrolyte is 0.5 M Na_2SO_4 aqueous solution, and the counter electrode, reference electrode, and working electrode are a platinum electrode, a calomel electrode, and an indium-tin-oxide (ITO) electrode coated with catalysts, respectively. The photoluminescence (PL) measurements of the samples were executed on an Edinburgh FLS1000 fluorescence spectrophotometer at room temperature with excitation wavelength of 365 nm. In situ DRIFTS of Mn_3O_4/Co_3O_4 were measured on Thermo Fisher Nicolet 6700 FTIR under UV-Vis irradiation. The samples were compacted to a piece in the in situ cell and pretreated in a He flows at 230 ℃ for 1 h to remove surface water and/or physically adsorbed oxygen. The toluene with a concentration of 500 ppm was injected into the gas chamber, which was balanced with N_2 or synthetic air.

2.4. Catalytic performance test

The evaluation of the toluene photothermal catalytic oxidation activities of the samples was carried out in a cylindrical stainless steel reactor (Fig. S1). A circular quartz window was on the top of the reactor for light penetration. 0.1 g catalysts were evenly spread on the porous sand core plate in the middle of the reactor through an 80-mesh sieve. The flow rate of the feed gas was 50 mL/min, which contained 500 ppm toluene and 20 vol% O_2, and the rest was balanced by N_2. A K-type thermocouple was contacted with the center of the catalyst surface for monitoring the actual temperature. The light source of the photothermal catalytic oxidation reaction of toluene is UV-Vis light (PLS-SXE300, Beijing Perfect light Technology Co. Ltd.). Before each photothermal catalytic reaction, the light intensity on the surface of catalysts was calibrated with an optical power meter (PL-MW2000, Perfect Light). The water vapor was carried into the reactor by a nitrogen stream, and the amount of water vapor was controlled by changing the flow of nitrogen and the temperature of the water bath. The toluene and the main oxide product CO_2 were analyzed by a gas chromatography (GC-2014 C, Shimadzu) and a CO_2 detector (PGA 650, Phymetrix). The conversion of toluene ($X_{toluene}$) and the yield of CO_2 were calculated by the following equations, respectively:

$$X_{toluene} = 100\% \times \frac{[\text{Toluene}]_{feed} - [\text{Toluene}]_{out}}{[\text{Toluene}]_{feed}} \tag{1}$$

$$CO_2 \text{ yield} = 100\% \times \frac{[CO_2]_{produced}}{7 \times [\text{Toluene}]_{feed}} \tag{2}$$

where $[\text{Toluene}]_{feed}$ and $[\text{Toluene}]_{out}$ represent the concentration of toluene in the feed gas and at the outlet of the reactor, respectively; $[CO_2]_{produced}$ represents the actual CO_2 concentration produced at the outlet.

The reaction rates ($r_{toluene}$) of toluene were calculated by the following equations [39]:

$$r_{toluene} = \frac{X_{toluene} \times C_{toluene}}{m_{cat.}} \tag{3}$$

where $C_{toluene}$ (μmol·min^{-1}) and $m_{cat.}$ (g) represent the mole flow rate of inlet toluene and the weight of catalyst, respectively.

2.5. Computational models and methods

The density functional theory (DFT) simulation was conducted by Vienna Ab initio Simulation Package (VASP, version 6.2.1) with projected augmented wave (PAW). The Perdew-Burke-Ernzerhof (PBE) function combined with the Hubbard model (GGA+*U*) was applied for generalized gradient approximation. The cut-off energy of the plane wave was set to 500 eV and the U_{eff} (i.e., U-J) of Co and Mn were set at 3.5 and 4 [14,71]. The width of the Gaussian smearing was set to 0.05 eV. A vacuum layer (15 Å) in the Z direction was used to separate the slab models.

For investigating the interfacial properties between Co_3O_4 and Mn_3O_4, two models for monomeric catalysts and two supported models for heterojunction catalysts were built (Fig. S2). Specifically, the four layers Co_3O_4 slab model was obtained by the reconstruction of Co_3O_4 (220) [2 × 2] supercell (11. 50 ×11.50 ×22.22 Å). The slab model for Mn_3O_4 with four layers was built by reconstructing Mn_3O_4 (211) [1 × 1] supercell (10.48 ×11.24 ×20.76 Å). For simulating the Co_3O_4 surface in composite Co_3O_4-Mn_3O_4, a supported-model $C_{Co/Mn}$ was built on Co_3O_4 (220) with $(Mn_3O_4)_2$ segment from Mn_3O_4 cell. Vice versa, the $C_{Mn/Co}$ was built on Mn_3O_4 (211) with $(Co_3O_4)_2$ segment from Co_3O_4 cell to simulate the Mn_3O_4 surface of Mn_3O_4-Co_3O_4. The bottom two layers of the models were fixed during geometrical optimization. A Gamma-Pack grid of 2 × 2 × 1 of k-points was employed in the geometrical optimization, which relaxed with a 0.02 eV/Å of maximum atomic forces and 10^{-5} eV of SCF tolerance. VASPKIT was used during the DFT simulation. The magnetic states of Mn and Co were set according to the literature [65,71].

The oxygen vacancy formation energy (E_{OV}) was defined as follows:

$$E_{OV} = E_{def} + 0.5\, E_{o_2} - E_{slab} \tag{4}$$

where E_{def} and E_{slab} are the total energy of slab with and without a oxygen vacancy, and E_{O_2} is the total energy of O_2 molecule in the gas phase.

The O_2 adsorption energy (E_{ads}) was estimated by:

$$E_{ads} = E_{slab-ads} - E_{o_2} - E_{slab} \tag{5}$$

where $E_{slab\text{-}ads}$ represent the total energy of the surface after oxygen adsorption.

The toluene adsorption energy ($E_{ads\text{-}tol}$) was estimated by:

$$E_{ads-tol} = E_{slab-tol} - E_{tol} - E_{slab} \tag{6}$$

where $E_{slab\text{-}tol}$ represents the total energy of the surface after toluene adsorption, and E_{tol} is the total energy of toluene molecule in the gas phase.

The work functions (Φ) was calculated as follows:

$$\Phi = E_{vac} - E_{Fermi} \tag{7}$$

where E_{vac} and E_{Fermi} represent the energy of vacuum level and Fermi level, respectively.

The free energy of the reaction steps before ring-opening was calculated by the formula:

$$\Delta G = \Delta E_{DFT} + \Delta E_{ZPE} - T\Delta S \tag{8}$$

where ΔE_{DFT} is the DFT electronic energy difference of each step, ΔE_{ZPE} is the correction of zero-point energy, ΔS is the variation of entropy, and T is the surface temperature of Mn_3O_4/Co_3O_4 under UV-Vis illumination ($T = 444$ K).

3. Results and discussion

3.1. Crystal structure and morphology

The crystal compositions and crystallographic structures of Mn-Co oxides were measured by XRD (Fig. 1). For single Mn oxide, the diffraction peaks at 18.0, 28.9, 30.9, 32.3, 36.1, 38.1, 44.4, 48.3, 49.9 50.8, 58.5, 59.9, and 64.6° are attributed to (101), (112), (200), (103), (211), (004), (220), (301), (204), (105), (321), (224), and (400) crystal planes of Mn_3O_4 (PDF#80–0832). In the synthesis of Mn-Co mixed oxides, when Co/Mn is less than 1, with the increase of Co content, it can be seen that the XRD peaks shift to the right and gradually form (Co, Mn)(Co, Mn)$_2$O$_4$-like spinel phase (PDF#18–0408) with diffraction peaks at 18.2, 29.3, 32.9, 36.4, 59.0, 60.7°, which is due to the ionic radius of Co^{2+} (0.72 Å) and Co^{3+} (0.69 Å) is smaller than that of Mn^{2+} (0.80 Å) and Mn^{3+} (0.72 Å), resulting in the replacement of some Mn ions by Co [86]. And when Co/Mn is larger than 1, the XRD diffraction peaks of the samples are gradually dominated by the characteristic peaks of Co_3O_4 (PDF#80–1541) as the Co content increases. Herein, the Co_3O_4 phase were 31.2, 36.8, 44.4, 59.3, and 65.2°, which were assigned to the (220), (311), (400), (511), and (400) facets. While for Mn_5Co_5, the coexistence of the characteristic peaks of Co_3O_4 (18.9, 31.2, 36.8, 44.8, 59.3, 65.2°) and Mn_3O_4 (36.1, 44.4, 58.5, 64.6°) indicate that Mn_5Co_5 is mostly a composite of Co_3O_4 and Mn_3O_4 (Mn_3O_4/Co_3O_4). SEM images showed the changes before and after the compounding of Mn_3O_4 and Co_3O_4. As shown in Fig. 2(a-c), the Mn_3O_4 presents polygonal lamellae with size greater than 100 nm, and the Co_3O_4 are clusters of spherical particles with sizes of 20–30 nm. While the Mn_3O_4/Co_3O_4 has the common characteristics of Mn_3O_4 and Co_3O_4, showing mixed morphology of flakes and particles. Furthermore, the N_2 adsorption-desorption isotherm in Fig. S3 was analyzed and the BET results listed in Table 1, which indicated that the Mn_3O_4/Co_3O_4 had smaller pore sizes, larger specific surface area, and increased pore volume compared to Mn_3O_4 and Co_3O_4. Additionally, the crystalline lattice size of Mn_3O_4/Co_3O_4 in the HRTEM images of Fig. 2(d) matched that of Co_3O_4 and Mn_3O_4 species. In particular, the lattice fringe of 0.246 nm corresponds to the (211) facet of Mn_3O_4, and the lattice fringe of 0.290 nm is ascribed to the (220) plane of Co_3O_4. Moreover, a clear phase interface boundary between Co_3O_4 and Mn_3O_4 can be observed (see the white line in Fig. 2(d)), and the Fourier transform diagram shows a distinct distortion of the lattice stripe, which indicates a strong interaction occurred between Co_3O_4 and Mn_3O_4 at the interface. Moreover, the detailed elemental distribution of Mn_3O_4/Co_3O_4 catalysts can be observed by EDS (Fig. 2(e-h)), in which the elements of Mn, Co, and O were uniformly distributed. This facilitated the formation of more homogeneous Mn-Co oxide interfaces.

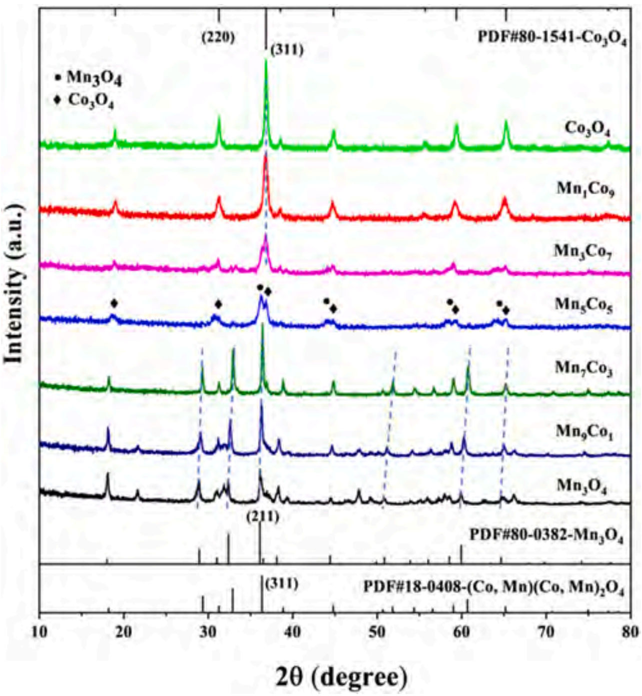

Fig. 1. XRD patterns of Mn_3O_4, Co_3O_4, and Mn_xCo_{10-x} mixed oxides.

The Raman spectrogram (Fig. S4) was further to analyze the bonding properties of Mn_3O_4/Co_3O_4. For Mn_3O_4, the strongest peak at 642 cm^{-1} is attributed to the symmetric stretching vibration of Mn (III, IV) [61]. Meanwhile, a series of characteristic Raman peaks at 191, 472, 513, 610 and 676 cm^{-1} could be observed in Co_3O_4, which are ascribed to the E_{2g}, E_g, F_{2g}, F_{2g}, and A_{1g} Raman-active modes of the Co_3O_4, respectively [86]. The spectrum of Mn_3O_4/Co_3O_4 displays two broad peaks at 480 and 609 cm^{-1}, where the former is attributed to Co-O-Co (E_g), and the latter may be caused by the left shift of the Mn-O (A_{1g}) characteristic peak of Mn_3O_4 [15,47]. Compared to the respective pure oxides, the strongest peaks become much wider, weaker, and even shift or disappear to some extent, which indicates a strong interaction between the two oxides near the interface, thus weakening the nearby Mn-O and Co-O bonds and causing a decrease in crystallinity and distortion of the lattice [5,42,47,87]. These results are also confirmed by XRD and TEM analyses (Fig. 1 and Fig. 2(d)). As such, oxygen mobility can be enhanced, thus making it easier to generate abundant oxygen vacancy defects around the interface, which in turn produced more reactive oxygen species to participate in the catalytic oxidation process [23].

3.2. Photothermal catalytic oxidation and thermal catalytic oxidation performances

The photothermal catalytic oxidation of toluene by a series of synthesized catalysts was investigated at a concentration of 500 ppm toluene and compared with the catalytic performance of individual metal oxides. As shown in Fig. S5-S6, the results showed that the toluene conversion and CO_2 yield exhibited the same trend of increasing and then decreasing with the increase of Mn/Co ratio in the above composite catalysts. It is noteworthy that the Mn_5Co_5 (called Mn_3O_4/Co_3O_4 in the text below) exhibited the highest toluene conversion and CO_2 mineralization rate, reaching 74.7% and 60.4% at 120 min, respectively. Compared to the single metal oxides of Co_3O_4 and Mn_3O_4 with 53.3% and 47.5% of toluene conversion, the catalytic performance of Mn_3O_4/Co_3O_4 was significantly enhanced. And the Mn_3O_4/Co_3O_4 has the highest reaction rate (Table 1). Based on the results of XRD and HRTEM that Mn_3O_4/Co_3O_4 was a heterogeneous structure composed of Mn_3O_4 and Co_3O_4, it was assumed that the catalytic performance enhancement may be due to the interaction between Mn_3O_4 and Co_3O_4. The composite $Mn_3O_4 + Co_3O_4$ (M+C) was obtained by mechanically mixing a certain ratio of Mn_3O_4 and Co_3O_4, which was calculated by the ICP results of Mn_3O_4/Co_3O_4 (Table 1). The photothermal catalytic performance of M+C was shown in Fig. 3(a-b), its toluene conversion was between that of Mn_3O_4 and Co_3O_4, and much lower than Mn_3O_4/Co_3O_4, speculating that the chemical interaction and interfacial effect between manganese and cobalt oxides are one of the main reasons for enhancing photothermal catalytic efficiency of Mn_3O_4/Co_3O_4. In addition, the performance of Mn_3O_4/Co_3O_4 is compared with other reported photothermal catalysts in the literature under similar reaction conditions in Table S1. In the UV-Vis irradiation range, Mn_3O_4/Co_3O_4 exhibits promising catalytic properties. Furthermore, a comparative experiment was conducted to compare the performance of Mn_3O_4/Co_3O_4 with that of

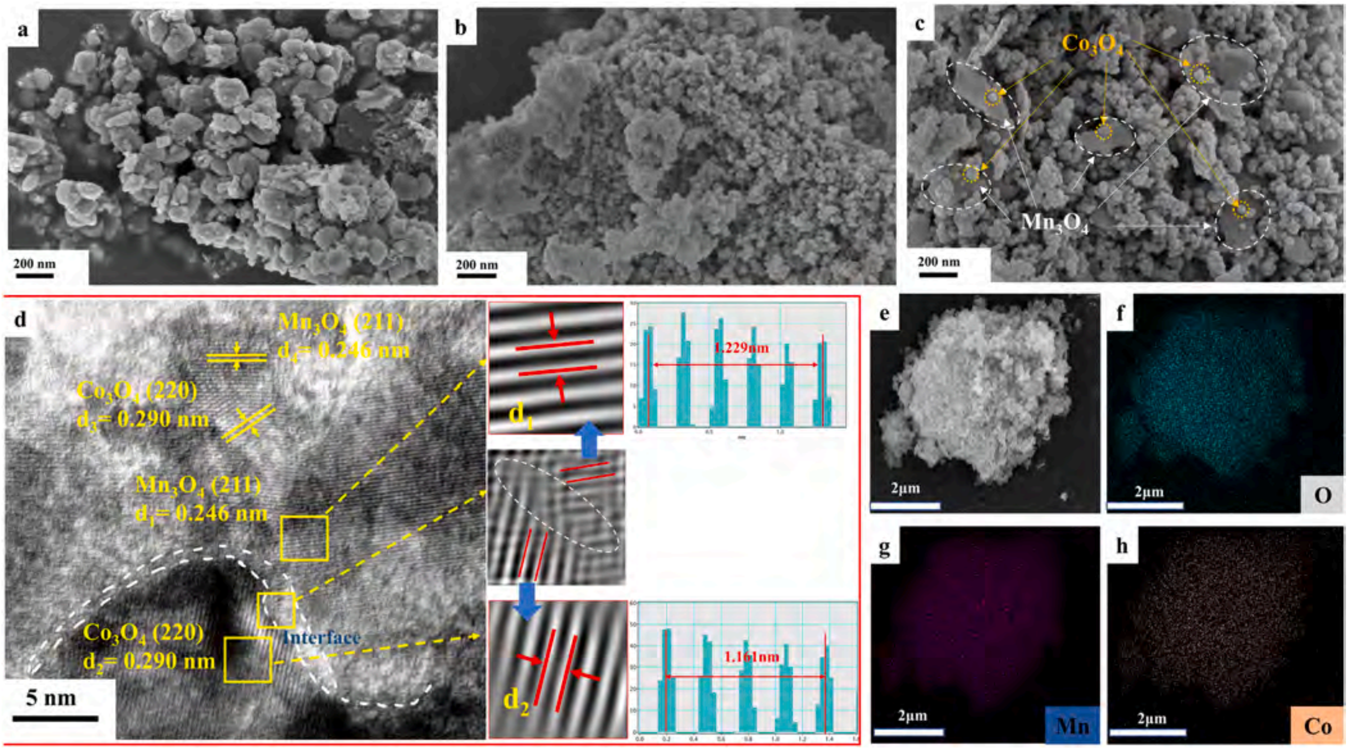

Fig. 2. (a-c) SEM of Mn_3O_4, Co_3O_4 and Mn_3O_4/Co_3O_4; (d) HR-TEM images of Mn_3O_4/Co_3O_4; (e-h) SEM image and the corresponding elemental mapping scan of Mn_3O_4/Co_3O_4.

Table 1

Elemental contents based on ICP measurement, BET surface area, and surface molar ratios based on XPS spectra of the Mn_xCo_{10-x} mixed oxides.

Catalyst	Element content (at %)[a]		Mn/Co		S_{BET}^{b} (m^2 g^{-1})	P_v^c (cm^3 g^{-1})	APD[d] (nm)	Surface molar ratio[e]				Reaction rates[f] (μmol g^{-1} min^{-1})
	Mn	Co	Experimental	Design				Mn^{4+}/Mn^{2+}	Mn^{3+}/Mn^{2+}	Co^{3+}/Co^{2+}	O_{ads}/O_{latt}	
Mn_3O_4	100	-	-	-	17.52	0.09	14.50	2.16	2.42	-	0.32	0.53
Mn_1Co_9	10.30	89.70	0.11	0.11	44.54	0.22	15.33	1.12	1.82	0.44	0.38	0.72
Mn_3Co_7	31.03	68.97	0.45	0.43	43.75	0.30	22.38	1.02	2.14	0.48	0.39	0.79
Mn_5Co_5	50.86	49.14	1.03	1.00	40.46	0.19	15.17	1.43	2.69	0.57	0.58	0.84
Mn_7Co_3	72.88	27.12	2.69	2.33	24.40	0.15	21.24	1.05	2.62	0.56	0.33	0.77
Mn_9Co_1	90.64	9.36	9.67	9	30.14	0.18	20.90	1.24	1.50	0.55	0.33	0.64
Co_3O_4	-	100	-	-	16.48	0.11	23.89	-	-	0.65	0.36	0.60

[a] Atom ratio from ICP-MS measurement.

[b] BET specific surface area.

[c] Total pore volume measured at $P/P_0 = 0.995$ isotherm using the BJH method

[d] Average pore diameter calculated form the BJH desorption branch.

[e] Calculated based on XPS spectra.

[f] Toluene reaction rate (in 120 min) of catalysts.

commercial TiO_2 (P25) catalysts. As shown in Fig. S7, the toluene conversion of P25 was significantly lower than that of Mn_3O_4/Co_3O_4 and deactivated rapidly. After a 2 h reaction, the P25′s color changed from white before to light yellow, presumably due to the rapid accumulation of intermediates on the surface.

To further investigate the difference between photothermal catalysis and thermal catalysis, the study of thermal catalytic oxidation toluene on Mn_3O_4/Co_3O_4, M+C, Mn_3O_4, and Co_3O_4 was conducted in a fixed bed (Fig. S1). The toluene concentration, flow rate, and catalyst amount in the thermal catalytic experiments were consistent with those in the photothermal catalytic experiments. The results were displayed in Fig. 3 (d) and Fig. S8. It was found that the Co_3O_4 exhibited the best thermal catalytic activity, while Mn_3O_4/Co_3O_4 showed the best photothermal activity. As seen in Fig. 3(d), the toluene conversion of Co_3O_4 is higher than that of Mn_3O_4/Co_3O_4 in the range above 160 °C. However, the temperature of Mn_3O_4/Co_3O_4 under illumination was lower than that of Co_3O_4 in the photothermal catalytic system (Fig. 3(c)). Theoretically, assuming that only a light-driven thermocatalytic reaction occurred in a photothermal catalytic system, the photothermal catalytic efficiency of Mn_3O_4/Co_3O_4 should be lower than that of Co_3O_4. However, the photothermal performance of Mn_3O_4/Co_3O_4 was significantly better than that of Co_3O_4, indicating that the introduction of light can not only provide heat but also induce photocatalysis or photoactivation of composite catalysts.

3.3. Surface property analysis of Mn-Co oxides heterojunction

To illustrate the reasons for the promotion of photothermal catalytic oxidation of toluene by Mn-Co oxides heterojunctions, the chemical states of the catalyst samples were detected by XPS and the analysis results are summarized in Table 1. The presence of Mn, Co, and O atoms in Mn_3O_4/Co_3O_4 was determined by XPS full spectrum in Fig. 4(a). As

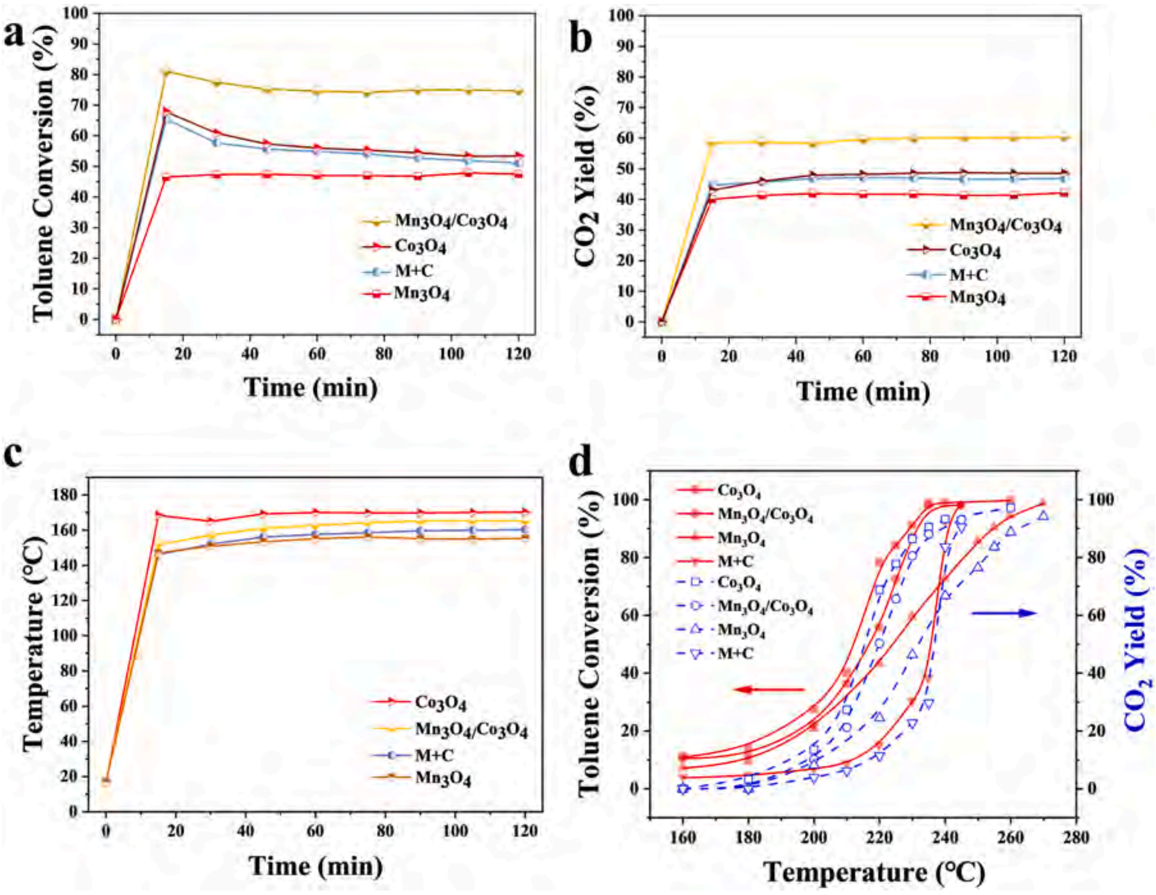

Fig. 3. (a-b) Photothermal catalytic performance of Mn_3O_4, Co_3O_4, Mn_3O_4/Co_3O_4, M+C; (c) catalyst surface temperature during photothermal catalysis reaction; (d) thermal catalytic performance of Mn_3O_4, Co_3O_4, Mn_3O_4/Co_3O_4, M+C. (Reaction conditions: 500 ppm toluene, 100 mg of catalyst, GHSV= 30,000 $mL\bullet g^{-1}\bullet h^{-1}$, light intensity of 822 mW/cm^2).

shown in Fig. 4(b), the XPS spectral peaks of O 1 s were used to analyze the oxygen species. Specifically, the peaks at the binding energies of 529.7–530.3 eV are the characteristic peaks of lattice oxygen (O_{latt}), the peaks at 531.1–531.3 eV are attributed to the adsorbed and dissociated reactive oxygen species (O_{ads}) near the oxygen vacancies, and the peaks at 532.9–533.6 eV are ascribed to the oxygen species (O_w) in the adsorbed molecular water [61,63]. In general, the large number of O_2 species adsorbed on the catalyst surface is associated with the capture of organic molecules and the activation of gaseous oxygen [43]. Moreover, surface-adsorbed oxygen species have better migration ability than lattice oxygen, which facilitates the catalytic oxidation reaction of VOCs [50]. The ratio of adsorbed oxygen to lattice oxygen (O_{ads}/O_{latt}) content for different Mn-Co oxides is given in Table 1. The Mn_3O_4/Co_3O_4 possesses the highest value of O_{ads}/O_{latt}, which was consistent with the excellent photothermal catalytic performance. Importantly, after the formation of Mn_3O_4/Co_3O_4 heterojunction, the peak of lattice oxygen in O 1 s shifted positively, which was attributed to the transfer of interfacial charge between Mn_3O_4 and Co_3O_4 hybridized the lattice oxygen of Mn_3O_4/Co_3O_4 and caused the electron density of lattice oxygen decreased [31,70]. Furthermore, in Fig. 4(c) and Fig. S9, the Mn $2p_{3/2}$ XPS spectra of Mn-Co oxides at 640.4 ± 0.4, 641.9 ± 0.3, and 643.8 ± 0.4 eV correspond to Mn^{2+}, Mn^{3+}, and Mn^{4+} species, respectively [53]. It should be noted that the ratio of Mn^{4+}/Mn^{2+} and Mn^{3+}/Mn^{2+} for Mn_3O_4/Co_3O_4 is the highest compared to other manganese cobalt composites (Table 1), and this further promotes its redox performance [69]. Meanwhile, in Fig. 4(d), the Co $2p_{3/2}$ XPS spectrum can be decomposed into four peaks with binding energies of 780 ± 0.3, 781.3 ± 0.3, 785.3 ± 0.2, and 789.3 ± 0.2 eV, corresponding to Co^{3+}, Co^{2+} species, and oscillatory satellite peaks associated with Co^{3+}, Co^{2+} substances, respectively [84]. As shown in Table 1, Co_3O_4 has the highest Co^{3+}/Co^{2+} ratio, while the ratio of Mn_3O_4/Co_3O_4 is slightly lower than that of Co_3O_4. In general, more Co^{3+} favors the complete oxidation of toluene [42]. Furthermore, we explored the relationship between the toluene conversion of Mn_xCo_{10-x} and the Mn, Co, O species. The trend curves of toluene conversion with the ratios of Mn/Co, O_{ads}/O_{latt}, $(Mn^{4+}+Mn^{3+})/Mn^{2+}$, and Co^{3+}/Co^{2+} for the Mn-Co series catalysts were summarized in Fig. S10, and the results showed that they were all volcanic in shape, indicating that the catalytic oxidation of toluene over Mn-Co oxides was strongly correlated with O_{ads}, Mn^{4+}, Mn^{3+}, and Co^{3+}, which was consistent with the literature reports [61].

H_2-TPR was employed to study the reduction property of the catalysts, and the results were presented in Fig. 5(a). For Mn_3O_4, the reduction peaks at 329 ℃ and 457 ℃ could be clearly observed, which corresponded to the reduction of Mn^{4+} to Mn^{3+} and Mn^{3+} to Mn^{2+}, respectively [20]. For Co_3O_4, the reduction peak at 277 °C corresponded to the reduction of Co^{3+} to Co^{2+}, and the broad peak ranged from 301° to 423°C was attributed to the reduction of Co^{2+} to Co^0 [89]. After the combination of Co_3O_4 and Mn_3O_4, the minimum reduction temperature of Mn_3O_4/Co_3O_4 showed a low-temperature shift relative to Mn_3O_4. Moreover, the peaks of the reduction of Co^{3+} to Co^{2+} and Mn^{4+} to Mn^{3+} overlapped as one broad peak at about 290 °C due to the stronger interaction between Mn_3O_4 and Co_3O_4, while the peaks appearing at 348 °C and 469 °C were attributed to the reduction of Co^{2+} to Co^0 and Mn^{3+} to Mn^{2+}, respectively [61]. In addition, a new peak was observed at 564 ℃, which could be related to the presence of Co-$[O]_x$-Mn coordination bonds [67]. As displayed in Fig. 5(a), the minimum reduction temperatures were in the order of $Co_3O_4 < Mn_3O_4/Co_3O_4 < Mn_3O_4$. In general, catalysts with lower reduction temperatures tended to exhibit

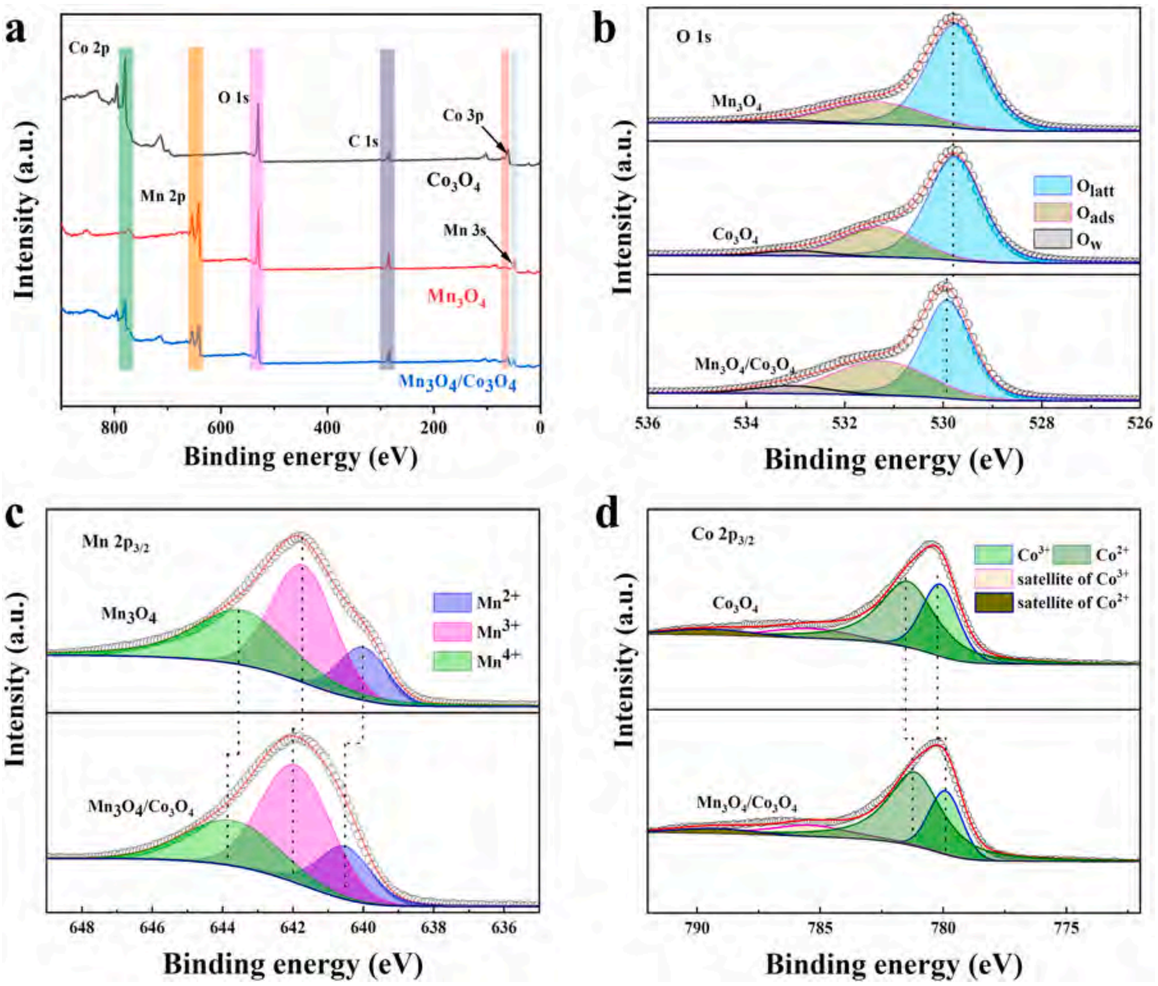

Fig. 4. (a) XPS survey spectrum and high-resolution XPS spectra of (b) O 1 s, (c) Mn $2p_{3/2}$ and (d) Co $2p_{3/2}$ of Mn_3O_4, Co_3O_4, and Mn_3O_4/Co_3O_4.

better redox properties, which was also evidenced by the order of T_{50} and T_{90} in the thermal catalytic oxidation of toluene (Fig. S8).

According to the results of previous Raman, TEM, and XRD characterization, the mismatch of different crystal lattices between heterojunctions tends to produce more structural distortion and thus vacancies nearby the interface [67]. The characteristic peak of EPR at $g= 2.003$ for dark conditions at room temperature is associated with single electron trapping vacancies, and the intensity of the peak is usually proportionate to the oxygen vacancy concentration [49,73]. As shown in Fig. 5(b), the Mn_3O_4/Co_3O_4 has the strongest peak intensity, followed by Co_3O_4, and Mn_3O_4 was basically invisible, indicating that the most oxygen vacancies were generated on Mn_3O_4/Co_3O_4. Generally, more oxygen vacancies mean that more gaseous oxygen species would be adsorbed and produce more reactive oxygen species, which was further verified by the fact that Mn_3O_4/Co_3O_4 shows the highest adsorbed oxygen content in the XPS results of O 1 s

To investigate the adsorption and activation of oxygen and the lattice oxygen migration ability of these Mn-Co oxides, O_2-TPD analysis was performed [7]. It is well known that oxygen species in materials include physisorbed oxygen (O_2), chemisorbed oxygen (α-species, O_2^-, O^-), surface lattice oxygen (β-species, O^{2-}) and bulk lattice oxygen (γ-species), as shown in Fig. 5(c), where α-species are related to the oxygen vacancy content and β-species are related to the lattice oxygen migration capacity [88]. As shown in Fig. 5(c-d). the oxygen desorption peak area of Mn_3O_4/Co_3O_4 is the largest at 100–400 °C, followed by Co_3O_4 and Mn_3O_4, which is attributed to that the Mn_3O_4/Co_3O_4 has the largest specific surface area and the most sites of chemically adsorbed oxygen. Moreover, the Mn_3O_4/Co_3O_4 presents a lower surface lattice oxygen desorption temperature (435 ℃), indicating that the surface lattice oxygen mobility of Mn_3O_4/Co_3O_4 is significantly enhanced compared to Mn_3O_4 and Co_3O_4. It is widely accepted that the oxidation of VOCs occurring on transition metal oxides mostly follows the Marse-van-Krevelen mechanism involving the participation of lattice oxygen in the redox cycle [55]. Herein, the better surface lattice oxygen mobility contributes to the deep oxidation of toluene.

In addition, based on different surface models, the formation energy of oxygen vacancies at the monomer oxide surface and heterojunction interface was calculated by DFT simulations. The surface models and the calculated oxygen vacancy formation energies are shown in Fig. 6. The E_{OV} of the Co_3O_4 slab and Mn_3O_4 slab were predicted to be 2.85 eV and 3.44 eV, respectively. While at the heterostructure interfaces of $C_{Co}/_{Mn}$ and $C_{Mn/Co}$, the E_{OV} were significantly weakened with − 0.95 and 1.93 eV, respectively. It is suggested that heterojunction oxide interfaces have higher surface lattice oxygen activity than pure oxides, resulting the oxygen vacancies being easily formed [52,67]. Moreover, according to the results of theoretical calculations, the sequence of forming oxygen vacancies from easy to difficult is as follows: $C_{Co}/_{Mn}$ (or $C_{Mn/Co}$) > Co_3O_4 > Mn_3O_4, which was consistent with oxygen vacancy concentrations measured by the EPR, XPS, and O_2-TPD.

3.4. *Energy band structure and S-scheme heterojunction*

In addition to the difference in the thermal catalytic capacity, the photoelectric properties also have a great influence on photothermal

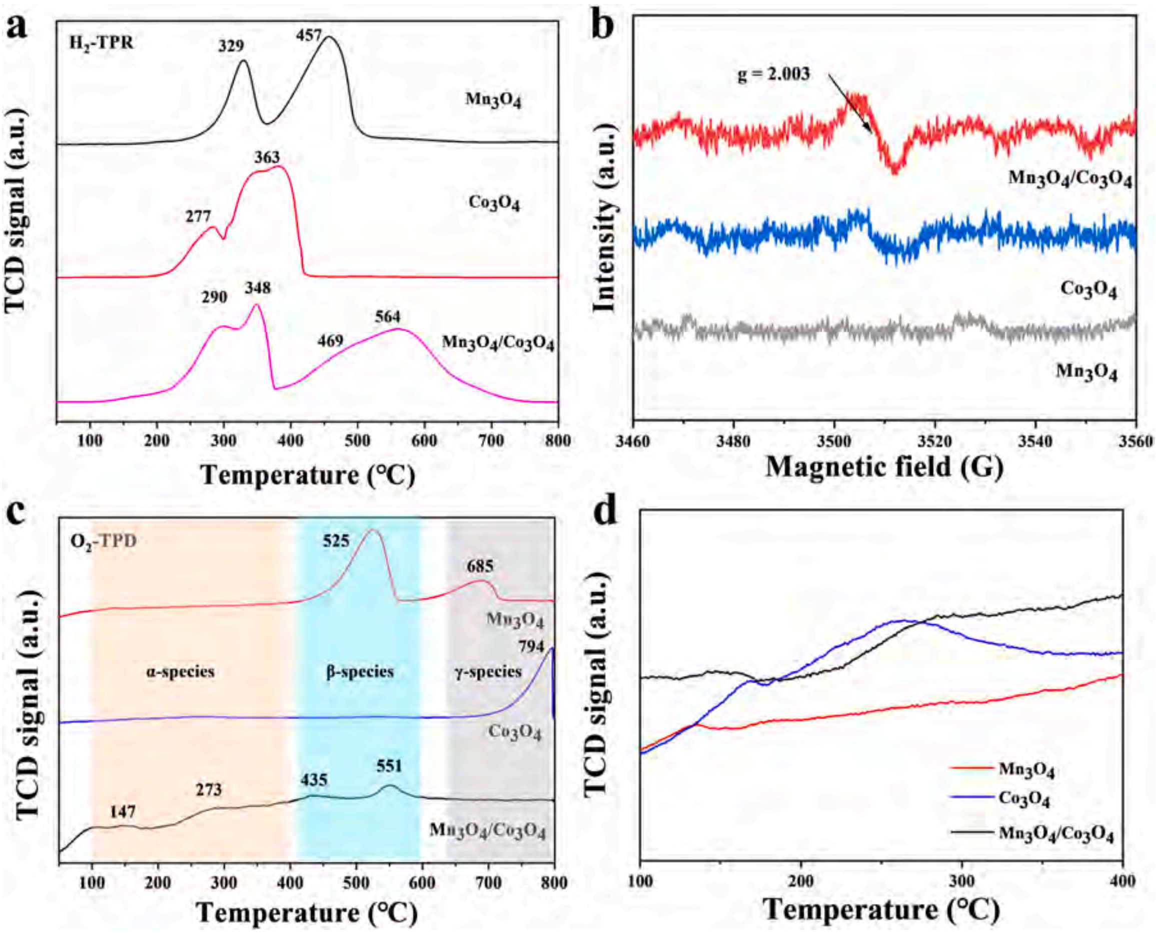

Fig. 5. (a) H_2-TPR of Mn_3O_4, Co_3O_4 and Mn_3O_4/Co_3O_4; (b) EPR spectrum of Mn_3O_4, Co_3O_4 and Mn_3O_4/Co_3O_4; (c) O_2-TPD of Mn_3O_4, Co_3O_4 and Mn_3O_4/Co_3O_4; (d) comparison of O_2-TPD intensities of Mn_3O_4, Co_3O_4 and Mn_3O_4/Co_3O_4 at 100–400 °C.

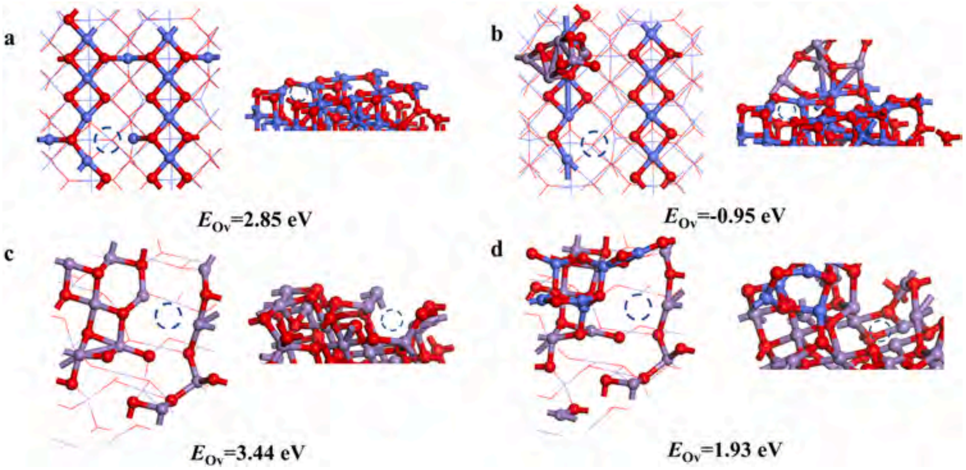

Fig. 6. Optimized structures with oxygen vacancies of (a) Co_3O_4 slab, (b) $C_{Co/Mn}$ model, (c) Mn_3O_4 slab, (d) $C_{Mn/Co}$ model (top view and side view).

catalytic activity. The optical property of Mn_3O_4, Co_3O_4, and Mn_3O_4/Co_3O_4 was detected by the UV-Vis diffuse reflectance spectra (DRS). As displayed in Fig. 7(a), the Mn_3O_4/Co_3O_4 and Co_3O_4 had a stronger light absorption capability compared to Mn_3O_4, which explained the fact that their surface temperature after illumination was higher than that of Mn_3O_4. Moreover, the curves of $(\alpha h\nu)^2$ versus light energy ($h\nu$) for the photocatalysts are presented in Fig. 7(b). According to the linear extrapolation method, the energy bandgap (Eg) of Mn_3O_4 and Co_3O_4 are 1.58 eV and 1.28 eV, respectively. Furthermore, according to the slope of the curve of the Mott-Schottky in Fig. 7(c-d), it could be concluded that the Mn_3O_4 and Co_3O_4 are p-type semiconductors. Meanwhile, their flat-band potential values of 0.67 V and 0.82 V (vs SCE, the standard calomel electrode) could be obtained according to the tangent of the Mott-Schottky, respectively. For p-type semiconductors, the valence band potential (Ev) is generally 0.1–0.2 V higher than their flat band potential, thus the Ev of Mn_3O_4 and Co_3O_4 can be calculated to be 0.77 V

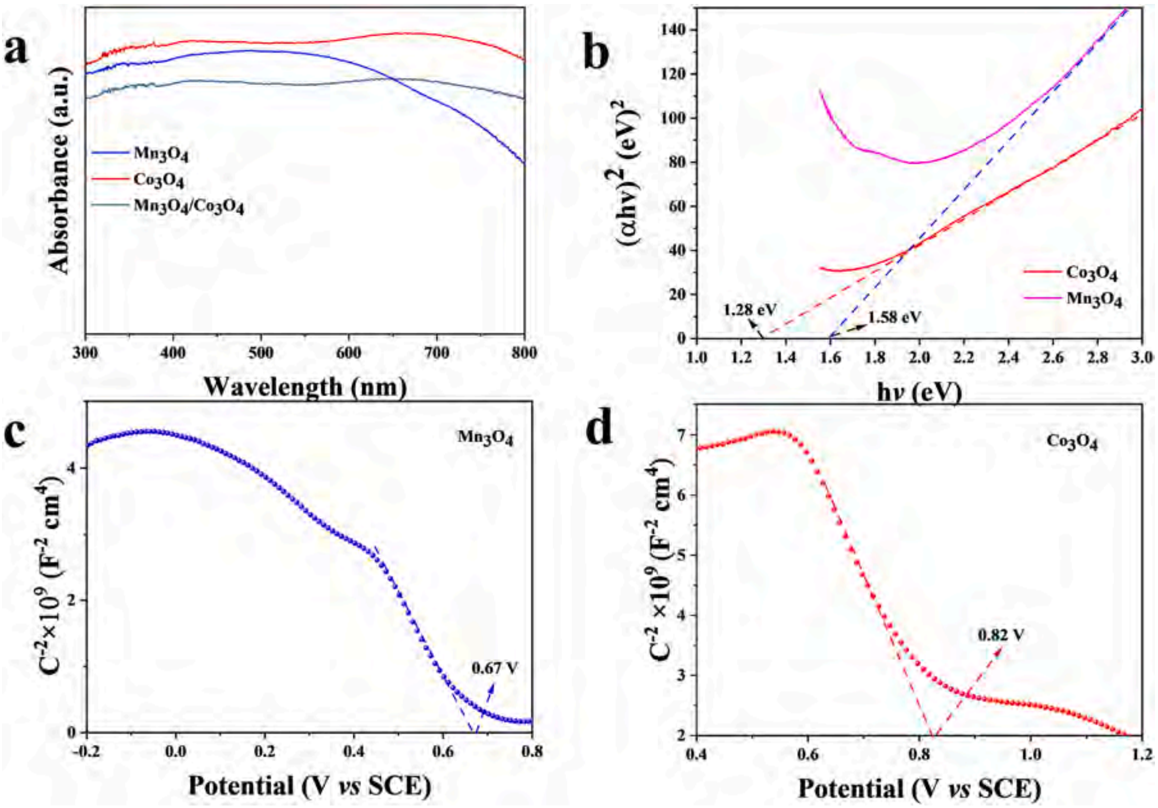

Fig. 7. (a) UV-Vis DRS of samples and Mn_3O_4, Co_3O_4 and Mn_3O_4/Co_3O_4; (b) plots of $(\alpha h\nu)^2$ against the photon energy for Co_3O_4 and Mn_3O_4; the Mott-Schottky plots of (c) Mn_3O_4 and (d) Co_3O_4.

and 0.92 V (vs SCE). On the basis of the Nernst equation: $E_{NHE} = E_{SCE} + 0.24$, the Ev of Mn_3O_4 and Co_3O_4 can be obtained to be 1.01 and 1.16 V (vs NHE, the normal hydrogen electrode) [22]. Then based on Ec=Ev-Eg, the conduction potential (Ec) of Mn_3O_4 and Co_3O_4 was − 0.57 V and − 0.12 V, respectively.

Theoretical calculations were used to further investigate the electron transfer between heterojunctions. Two loaded models $C_{Mn/Co}$ and $C_{Co/Mn}$ were used to analyze the surface properties of Mn_3O_4-Co_3O_4 and Co_3O_4-Mn_3O_4. The electron transfer from Mn_3O_4 to Co_3O_4 can be determined by the phenomenon of electron aggregation and transfer on the Co_3O_4 side in the charge difference density diagram of Fig. 8(a-b), and this conclusion is further corroborated by the Bader charge analysis. Specifically, in the $C_{Co/Mn}$ model, the overall increased electron in the Co_3O_4 part is 1.81 electrons compared to the pure Co_3O_4, while in the $C_{Mn/Co}$ model, the overall increased electron in the Co_3O_4 part is 0.26 electrons compared to the monomeric Co_3O_4. These trends are

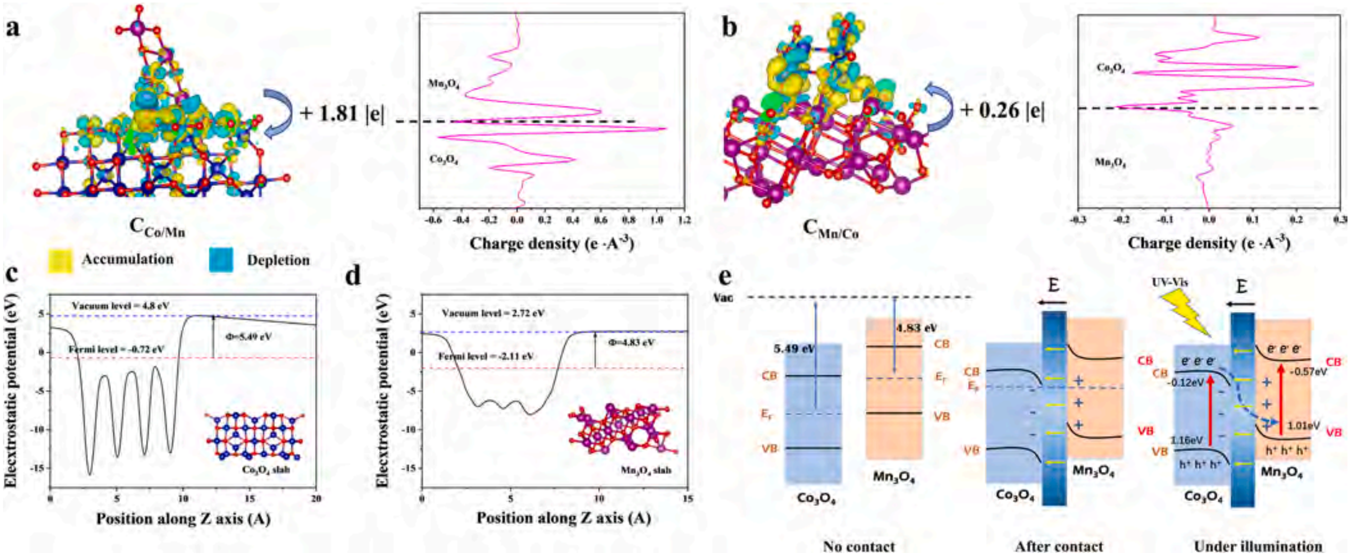

Fig. 8. (a-b) Charge difference distribution between Mn_3O_4 and Co_3O_4 with the corresponding planar average charge density plot for the $C_{Co/Mn}$ and $C_{Mn/Co}$ models (sideview); The average potential profile along Z axis direction of (c) Co_3O_4 and (d) Mn_3O_4 slabs; (e) Scheme of the formation mechanism of S-type heterogeneous junction.

consistent with the shifts of the Mn species toward higher binding energies and the Co species toward lower binding energies for Mn_3O_4/Co_3O_4 in Fig. 4(c-d). Furthermore, the Fermi energy levels (E_F) and work functions (Φ) of Co_3O_4 and Mn_3O_4 could be obtained by theoretically calculating their respective average potentials in the Z-axis direction. As shown in Fig. 8(c-d), the E_F values of Co_3O_4 and Mn_3O_4 were calculated to be − 0.72 eV and − 2.11 eV, respectively. Meanwhile, 5.49 eV and 4.83 eV of Φ values were obtained for Co_3O_4 and Mn_3O_4, respectively. Since Co_3O_4 had the lower E_F, when Mn_3O_4 contacted with Co_3O_4, the electrons of Mn_3O_4 flowed to Co_3O_4, and the energy bands of Mn_3O_4 and Co_3O_4 were bent upward and downward respectively. Thus, an internal electric field was formed at the heterojunction interface from Mn_3O_4 toward Co_3O_4 (left and middle in Fig. 8(e)) [92].

Combined with the previous energy band structure analysis and theoretical calculations, it can be speculated that photogenerated electrons and holes are generated in Mn_3O_4 and Co_3O_4 under UV-Vis light excitation. With the synergistic effects of energy band bending, directional electric field, and Coulomb force, the photogenerated electrons in the conduction band of the Co_3O_4 compound with the valence band photogenerated holes of Mn_3O_4. Eventually, the conduction band electrons of Mn_3O_4 and the valence band holes of Co_3O_4 are retained. In this way, the S-scheme heterojunction was formed, just as shown on the right in Fig. 8(e), which can maintain the maximum redox capacity of photogenerated charge carriers.

The interaction of semiconductor materials and photons induces the generation of excited state electron and hole pairs to participate in the photochemical reaction processes. Many previous reports have demonstrated that photocatalytic degradation of organic pollutants can be achieved by direct oxidation of holes or indirect oxidation of hydroxyl radicals formed by photoexcited hole oxidation of water molecules ($H_2O + h^+ \rightarrow H^+ + \cdot OH$) and superoxide radicals generated by photoexcited electron reduction of molecular oxygen ($O_2 + e^- \rightarrow \cdot O_2^-$) [1]. To further verify whether the catalyst produced active substances under light illumination, EPR spectroscopy was used for free radical detection. The samples were respectively dispersed in methanol and deionized water, and DMPO was added to the suspensions to detect $\cdot O_2^-$ and $\cdot OH$. Theoretically, the conduction band potential of Mn_3O_4 (−0.57 eV) is higher than the redox potential of $O_2/\cdot O_2^-$ (−0.33 eV), thus $\cdot O_2^-$ radicals could be formed under photoexcitation. Fig. 9(a) showed that the characteristic signal of $\cdot O_2^-$ radicals were indeed observed, while there was no signal on Co_3O_4. It was noteworthy that the signal of $\cdot O_2^-$ was further enhanced on Mn_3O_4/Co_3O_4, indicating that more photogenerated electrons react with oxygen, suggesting that the heterojunctions reduced the compounding of photogenerated carriers [34]. In contrast, in Fig. 9(b), all the samples could not produce the quadruple characteristic signal peaks of $\cdot OH$ radicals after illumination, which was due to their valence band potentials being lower than the redox potential of $H_2O/\cdot OH$.

In addition, the irregular coordination of heterometallic elements with oxygen atoms at the heterojunction interface could change the local electronic state and affect the adsorption and activation of reactant molecules [21]. The adsorption and activation of oxygen at the heterogeneous interface was further investigated by DFT calculations (Fig. S11). All heterogeneous models present higher adsorption energies

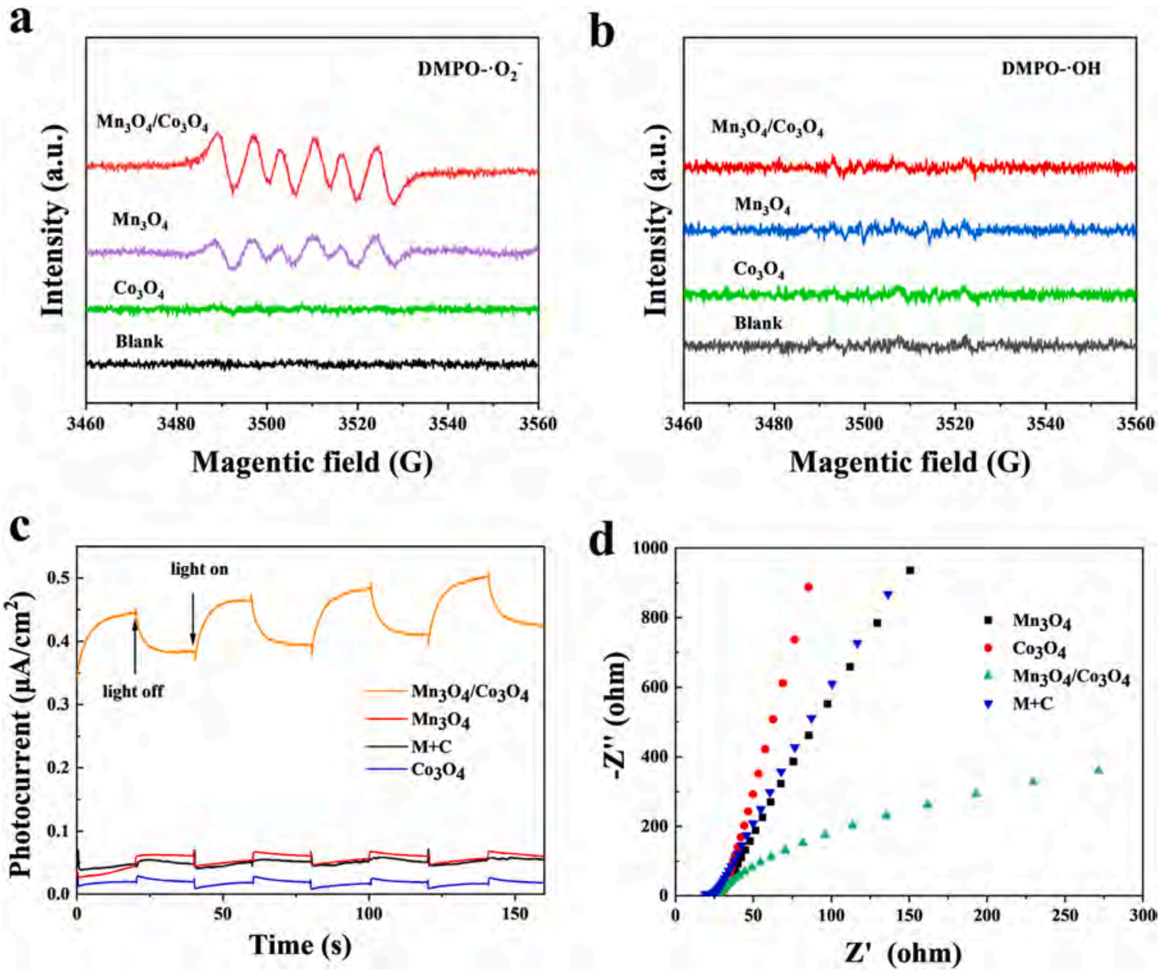

Fig. 9. (a) ESR spectra of DMPO-$\cdot O_2^-$ and (b) DMPO-$\cdot OH$ of Mn_3O_4, Co_3O_4, and Mn_3O_4/Co_3O_4 under UV-Vis illumination; (c) photocurrent responses and (d) EIS spectra of Mn_3O_4, Co_3O_4, Mn_3O_4/Co_3O_4, and M+C samples.

of oxygen compared to their pure slabs. In particular, the oxygen adsorption energy at the Co_3O_4 (220) surface was − 0.91 eV and the bond length of oxygen was 1.21 Å. After compounding with Mn_3O_4, the adsorption energy of oxygen at the heterogeneous interface decreased to − 1.31 eV and the bond length of oxygen increased to 1.32 Å, indicating that oxygen at the heterogeneous interface was more easily adsorbed and activated by the combined effect of Co_3O_4 and Mn_3O_4. Similarly, the oxygen adsorption energy at the $C_{Mn/Co}$ interface decreased significantly from 0.38 eV to − 3.51 eV compared to that of pure Mn_3O_4 (211) surface, and the oxygen bond length increased from 1.28 Å to 1.35 Å. The bond length of the activated oxygen molecule was close to 1.33 Å of $\cdot O_2^-$, which further indicated that the heterogeneous structure was conducive to lowering the oxygen adsorption energy and activating oxygen molecules into reactive oxygen species for participating in oxidation reactions [18,9].

Furthermore, the ability of Mn_3O_4/Co_3O_4 heterojunction in photogenerated charge separation and electron transfer was investigated by transient photocurrent response and EIS tests. It could be seen in Fig. 9(c), the intensity of photocurrent on Mn_3O_4/Co_3O_4 was much higher than Mn_3O_4 and Co_3O_4, indicating that Mn_3O_4/Co_3O_4 heterojunction had excellent photo-induced carriers separation and charge migration ability [81]. In general, the smaller diameter Nyquist curve implied a lower resistance, which facilitated the transfer and separation of the photogenerated electron-hole [29]. As presented in Fig. 9(d), the Nyquist of Mn_3O_4/Co_3O_4 exhibited a smaller diameter compared to Mn_3O_4 and Co_3O_4, suggesting easier charge transfer [57]. It should also be particularly noted that the photocurrent intensity of M+C was not significantly different from that of the monometallic oxides, and the radius of the Nyquist pot was between Mn_3O_4 and Co_3O_4, indicating that the physically mixed metal composite oxides were not able to enhance their photoelectrochemical properties. Moreover, the PL emission spectra of Mn_3O_4, Co_3O_4, and Mn_3O_4/Co_3O_4 were carried out under the same conditions to further investigate the effect of heterostructure on the recombination rate of photogenerated carriers [35]. Generally, the height of the PL curve is directly proportional to the recombination rate [3]. As illustrated in Fig S12, the PL intensity of Mn_3O_4/Co_3O_4 is significantly lower than that of Mn_3O_4 and Co_3O_4, suggesting the S-scheme heterojunction structure can delay the rapid compounding of photogenerated electron-hole pairs and improve the photocatalytic performance [33].

3.5. *Oxygen transient response and in situ DRIFTS experimental study*

The reaction mechanism and intermediates of toluene by photothermal catalytic oxidation of Mn_3O_4/Co_3O_4 were investigated by the transient response and in situ DRIFTS experiments. The results of photothermal oxidation of toluene over Mn_3O_4/Co_3O_4 with different feed gas were presented in Fig. 10(a). It could be noticed that the conversion of toluene is maintained at 73.0% under air atmosphere. However, when replacing air with nitrogen, the toluene conversion and the CO_2 yield decreased dramatically. After the reaction for 135 min in Toluene/N_2 atmosphere, the outlet concentration of toluene was almost the same as the inlet concentration, and CO_2 is undetectable in the exhaust gas. The phenomenon that the oxidation of toluene still occurs gradually over time in the absence of gaseous oxygen indicates that the chemisorbed oxygen or the reactive oxygen species generated under light or reactive lattice oxygen of Mn_3O_4/Co_3O_4 may react with toluene. Once the toluene/N_2 flow was cut off and toluene/Air was re-introduced, the toluene conversion and CO_2 yield returned sharply to the level before the nitrogen was introduced. It suggests that the gaseous oxygen can replenish the above depleted reactive oxygen species and the oxidation rate of toluene with the participation of large amounts of gaseous oxygen was higher than the reaction rate with the participation of limited oxygen species.

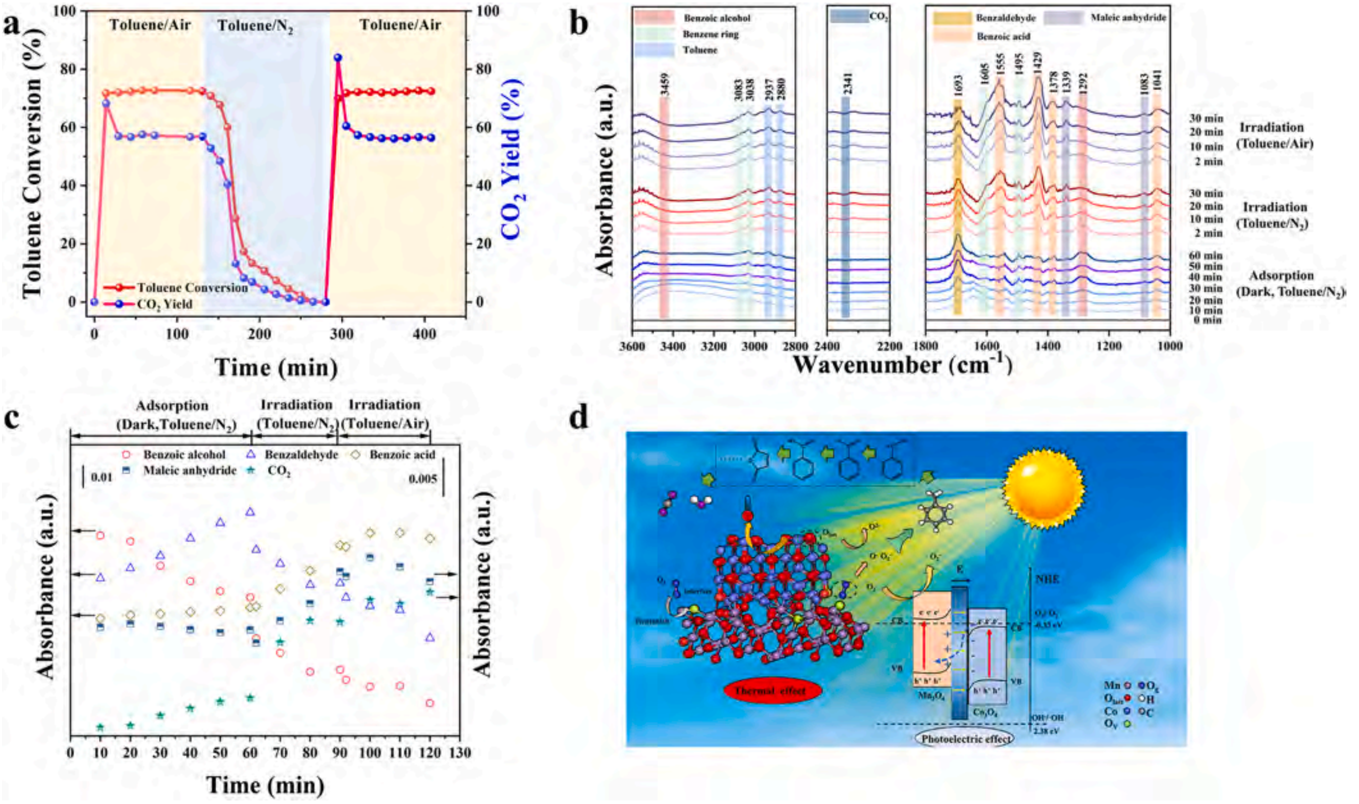

Fig. 10. (a) Oxygen transient response performance of Mn_3O_4/Co_3O_4; (b) time-dependent in situ DRIFTS spectra of Mn_3O_4/Co_3O_4 with 500 ppm toluene under UV-Vis using N_2 or synthetic air as balance gas; (c) the variation of infrared absorption intensity of toluene oxidation intermediates with in situ testing time; (d) mechanism of toluene photothermal catalytic oxidation over Mn_3O_4/Co_3O_4 under UV-Vis illumination.

The in situ DRIFTS experiment was further employed to investigate the conversion pathways of intermediates during the adsorption of toluene on Mn_3O_4/Co_3O_4 and photothermal oxidation in different gas atmospheres (Fig. 10(b)). The characteristic infrared absorption peaks of various intermediates are summarized in Table S2. At first, the sample was adsorbed with 500 ppm toluene/N_2 for 60 min under dark conditions. Several absorption peaks were observed in the region of 3600–2800 cm^{-1} and 1800–1000 cm^{-1}. Among them, the band located at 3083 and 3038 cm^{-1} are attributed to the unsaturated C-H vibrations on aromatic rings and the peaks at 2937 and 2880 cm^{-1} are assigned to symmetric and asymmetric vibrational peaks of C-H bonds of benzyl methyl groups [11,26]. Moreover, the peaks at 1605 and 1495 cm^{-1} are vibrational characteristic bands of aromatic ring C═C bonds [26]. This indicates the presence of adsorbed toluene on the surface of the catalyst. During the first 20 min of toluene adsorption, significant absorption bands were immediately observed at 3459 and 1292 cm^{-1}, which are characteristic of benzyl alcohol (hydroxyl O-H and C-O stretching vibrations) [11,49]. Then the intensity of the peak at 3459 cm^{-1} gradually decreased with time, while the peak of 1693 cm^{-1} representing benzaldehyde began to increase significantly over time, suggesting that the methyl group on toluene was destroyed to form benzyl alcohol by the chemically adsorbed oxygen and surface lattice oxygen of the catalyst and then rapidly oxidized to benzaldehyde [10]. When the Xe lamp was turned on after toluene adsorption under an N_2 atmosphere for 60 min, some new peaks appeared and strengthened gradually with the irradiation time along with the gradual decrease of the characteristic peak of benzaldehyde. The bands at 1555, 1429, and 1378 cm^{-1} were ascribed to symmetric and asymmetric stretching vibration peaks of the carboxylic C═O bond, and the peak at 1041 cm^{-1} may be also assigned to the C-O bond vibration peak in carboxylic acids, indicating the formation of benzoic acid species [10,11,72]. In addition, the appearance of the peaks at 1339 and 1083 cm^{-1} indicated the production of maleic anhydride [52,68]. The weak adsorption peak located at 2341 cm^{-1} corresponded to the O═C═O bond asymmetric stretching vibration of CO_2 [26,39]. It suggested that illumination could drive the lattice oxygen in the catalyst to further oxidize benzaldehyde to benzoic acid, maleic anhydride, and CO_2 even in the absence of gaseous oxygen, which coincided with the phenomenon of oxygen transient response experiment. With the introduction of air after 30 min of reaction in a nitrogen atmosphere, it was found that the intensities of the characteristic peaks of benzaldehyde were obviously reduced and the intensities of characteristic peaks for benzoic acid, maleic anhydride, and CO_2 were further enhanced. This is because the introduction of oxygen can form superoxide radicals under illumination and replenish the chemisorbed oxygen and reactive lattice oxygen of catalysts consumed in the oxygen-free catalytic stage, allowing the intermediates accumulated on the catalyst surface to be further oxidized. Moreover, the variation of the intensities of the characteristic peaks of the intermediates (3459 cm^{-1}, benzyl alcohol; 1693 cm^{-1}, benzaldehyde; 1555 cm^{-1}, benzoic acid, 1339 cm^{-1}, maleic anhydride; 2341 cm^{-1}, CO_2) with time during the whole in situ DRIFTS experiment was normalized and presented in Fig. 10(c). Specifically, the characteristic peak of benzyl alcohol decreases in intensity throughout the adsorption-reaction process. The peaks of benzaldehyde were continuously generated on the catalyst surface during the adsorption process and decreased rapidly after the light was turned on. Meanwhile, the characteristic peaks of benzoic acid and maleic anhydride accumulated rapidly after the light was turned on and started to decrease after 10 min of oxygen introduction, indicating that the intermediates were continuously oxidized and decomposed in the oxygen-containing atmosphere, which was also proved by the gradual increase of CO_2 peaks. The trends of the intensities of the characteristic peaks of various intermediates indicated that the photothermal catalytic reaction pathway of toluene over Mn_3O_4/Co_3O_4 may proceed in the following steps: toluene → benzyl alcohol → benzaldehyde → benzoic acid → maleic anhydride → H_2O and CO_2.

Additionally, DFT calculations were conducted to explore the potential mechanism for the enhanced photothermal catalytic performance of Mn_3O_4/Co_3O_4. Specifically, to understand the adsorption effect of heterogeneous interfaces towards toluene, the adsorption models of toluene on the surfaces of Mn_3O_4, Co_3O_4 and interfaces of their composite structure were constructed as shown in Fig. S13. It was obvious that all the composite structures showed higher adsorption energies compared to their respective monomeric oxides, indicating that the introduction of heterogeneous structures could enhance the adsorption of toluene. Moreover, the adsorption capacity for toluene followed this order Mn_3O_4 (−0.75 eV) < Co_3O_4 (−1.16 eV) < Mn_3O_4/Co_3O_4 (−1.47/−2.01 eV). These calculations were also confirmed by the results of the toluene-TPD tests in Fig. S14. Among them, Mn_3O_4/Co_3O_4 had the highest toluene adsorption capacity and desorption temperature, Co_3O_4 was the second and Mn_3O_4 was the smallest.

Numerous studies have confirmed that benzoic acid is a key intermediate in the mineralization of toluene, which is the beginning of an effective ring-opening reaction [6,8,83]. Based on the results of in situ DRIFTS, the free energy change of the conversion path of toluene → benzyl alcohol → benzaldehyde → benzoic acid at the $C_{Mn/Co}$ and $C_{Co/Mn}$ interfaces were calculated. It could be seen from Fig. S15, the conversion from toluene to benzoic acid over the $C_{Co/Mn}$ surface is a thermodynamic energy-decreasing process, indicating that toluene is easily converted to benzoic acid. However, on the $C_{Mn/Co}$ surface, the conversion of benzyl alcohol to benzaldehyde is a free energy-lifting process, indicating that more external energy needs to be provided to induce the reaction to proceed. The difference in the ease of conversion of benzoic acid at the $C_{Mn/Co}$ and $C_{Co/Mn}$ interfaces also indirectly explains the low overall mineralization rate of Mn_3O_4/Co_3O_4.

To summarize, the detailed photothermal catalytic reaction mechanism of toluene occurring on Mn_3O_4/Co_3O_4 under UV-Vis illumination was shown in Fig. 10(d). An S-scheme heterojunction of Mn_3O_4/Co_3O_4 was formed between Mn_3O_4 and Co_3O_4, and due to the lattice mismatch, oxygen vacancies are more easily formed nearby the heterojunction interface. The oxygen vacancies facilitate the adsorption and activation of oxygen in the air to form reactive oxygen species (O^-, O_2^-) and improve the mobility of lattice oxygen (O^{2-}), which in turn participates in the toluene oxidation process under thermal drive. Moreover, the heterogeneous interface further enhances the adsorption of toluene, thus contributing to the photothermal degradation of toluene. In addition, due to the energy band bending and the built-in electric field, the photogenerated electrons on the CB of Co_3O_4 and the holes on the VB of Mn_3O_4 compounded, which promoted charge transfer and inhibited the complexation of photogenerated electrons and holes on Mn_3O_4 and Co_3O_4. As a result, the higher CB and lower VB of the composite catalyst were retained, the photogenerated electrons generated on the CB of Mn_3O_4 reacted with air to form super oxygen radicals ($\cdot O_2^-$), and the holes of Co_3O_4 VB could also participate in the toluene oxidation process as active substances. Overall, the photothermal degradation of toluene under UV-Vis light irradiation follows the conversion pathway (toluene → benzyl alcohol→ benzaldehyde → benzoic acid → maleic anhydride → H_2O and CO_2) through the synergistic effect of thermal and photoelectric effects on Mn_3O_4/Co_3O_4.

3.6. *Durability, water resistance, cycling stability, and performance under different operating conditions*

Considering that the CO_2 conversion of Mn_3O_4/Co_3O_4 was only 60% in Fig. 3(b), it was speculated that there might be many intermediate products on its surface. In addition to the intermediates deposited on the catalyst surface observed by in situ DRIFTS, the presence of some cyclic hydrocarbons, benzene, and lipids in the tail gas was detected by using GC-MS (Fig. S16 and Table S3). This indicates that the products in the toluene oxidation process are very complex and may be accompanied by interactions between the intermediates. To test the catalyst's ability to resist carbon accumulation, a long-cycle stability experiment was carried out. The Fig. 11(a) showed that the catalytic performance of

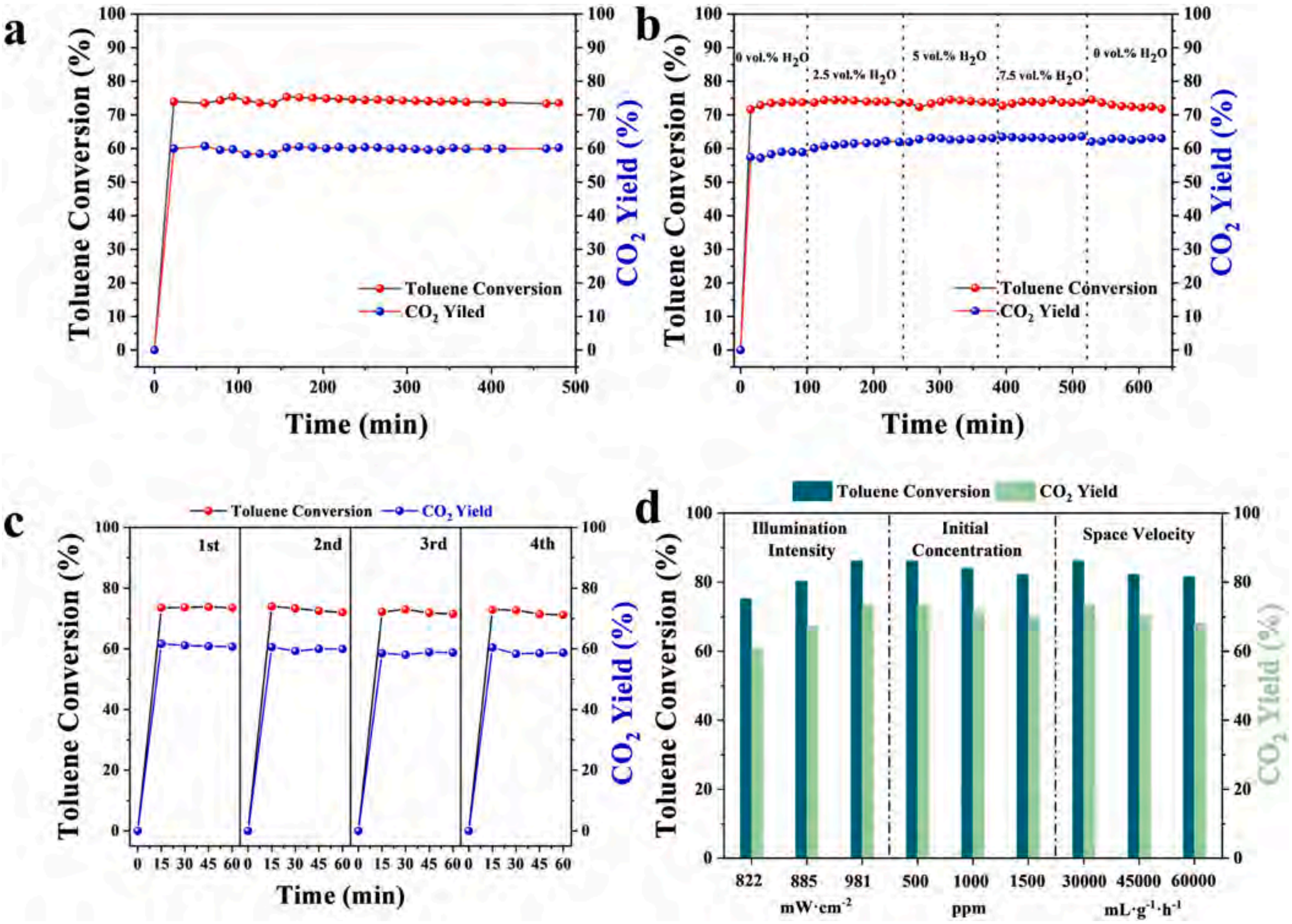

Fig. 11. (a) Stability test, (b) water resistance, (c) cyclic stability of Mn_3O_4/Co_3O_4, and (d) performance of photothermal catalytic oxidation of toluene under different operating conditions.

Mn_3O_4/Co_3O_4 could remain stable for nearly 500 min despite the limited conversion of CO_2. Generally, the process of VOCs actual emission is often accompanied by the presence of water vapor, which has an important influence on the catalytic performance. Thus, the gradient water resistance performance of Mn_3O_4/Co_3O_4 was also investigated, as shown in Fig. 11(b). With the successive introduction of 2.5 vol%, 5 vol %, and 7.5 vol% water vapor, the conversion of toluene remained essentially unchanged, while the conversion of CO_2 increased slightly. And even after the water was cut off, the conversion of CO_2 at 635 min (62.9%) was still higher than that before the addition of water (58.8%). It is speculated that the introduction of water vapor may have produced an activation effect, where the intermediate products were favorably converted to CO_2 under wet conditions [78]. It also indicated that the competing adsorption effect of water was not obvious on the Mn_3O_4/Co_3O_4 surface and did not cause a decrease in the toluene conversion rate. Therefore, Mn_3O_4/Co_3O_4 exhibited good water resistance. In addition, the cycling stability of the catalyst was tested by turning off the light for half an hour after turning on the light for one hour and operating it four times in succession. From Fig. 11(c), it could be observed that the Mn_3O_4/Co_3O_4 has good cycling stability and its photothermal catalytic performance did not change significantly after four cycles of use, which offers possibilities for practical applications.

To further explore the potential of Mn_3O_4/Co_3O_4 for practial applications, we also investigated the effects of different operating conditions on the catalytic performance, including light intensity, toluene initial concentration and space velocity. As shown in Fig. 11(d), the toluene conversion and CO_2 yield were enhanced with increasing light intensity. It is because higher light intensity will further increase the reaction temperature and photon flux, more easily inducing thermocatalysis and exciting more electrons to form free radicals [19]. Furthermore, the conversion of toluene gradually decreased with the increase of the initial concentration of toluene under 981 mW/cm^2 Xe lamp irradation, which was due to the limited active sites of the catalyst and the competition between toluene adsorption [12,51]. Similarly, the toluene conversion also showed a gradual decrease when the space velocity was increased. This is because that the higher the air velocity, the shorter the residence time of toluene on the catalyst surface, which tends to cause incomplete oxidation of toluene [46]. However, the Mn_3O_4/Co_3O_4 showed little change in the conversion of toluene in the range of 500–1500 ppm initial concentration and 30,000–60,000 $mL{\cdot}g^{-1}{\cdot}h^{-1}$ space velocity, indicating that Mn_3O_4/Co_3O_4 has excellent operational flexibility.

4. Conclusion

In conclusion, effective Mn_3O_4/Co_3O_4 heterojunction catalysts were synthesized through a facile hydrothermal co-precipitation method. The obtained Mn_3O_4/Co_3O_4 sample showed favorable photothermal catalytic performance, which can remove 74.7% continuous state toluene under UV-Vis light irradiation. Importantly, the toluene conversion efficiency was 21.4% and 27.2% higher than that of pure Co_3O_4 and Mn_3O_4, respectively. It is considered that the interfacial effect leads to the larger surface area, the higher ratio of Mn^{4+}, Mn^{3+}, and Co^{3+} species, and better low-temperature redox capability of Mn_3O_4/Co_3O_4, which contributed to the photothermal catalytic performance.

Furthermore, according to the results of structural characterization and theoretical calculations, the heterojunction interfaces tended to cause more oxygen defects and also tend to adsorb and activate oxygen molecules. More importantly, an S-scheme heterojunction was formed between Mn_3O_4 and Co_3O_4 due to different work functions and energy band bending. Therefore, UV-Vis light irradiation can both accelerate the electron transfer between the heterogeneous interfaces and reduce the recombination of photogenerated carriers, and retain the high redox capacity to generate more reactive oxygen species, thus further promoting the photothermal catalytic reaction. In addition, in situ DRIFTS analysis revealed the mechanism of the photothermal catalytic oxidation of toluene over Mn_3O_4/Co_3O_4 and identified the conversion pathway. It was expected that the design and construction of narrow-band semiconductor heterojunctions rich in interfacial defects and unique energy band structures was an important inspiration for photothermal synergistic catalytic removal of VOCs.

Environmental Implication

As a typical VOC, toluene is widely used in the construction and dyeing industries. However, it is harmful to the human respiratory and central nervous systems. Moreover, it is an important precursor to the formation of ozone and $PM_{2.5}$, which are potentially more hazardous to the environment. Therefore, it is an urgent task to remove toluene waste gas. In this work, the efficient photothermal catalytic degradation of toluene was achieved on the Mn_3O_4/Co_3O_4 composite, which couples light's thermal and photoelectric effects by the interfacial effect. It provides an innovative strategy for the design of photothermal catalysts.

CRediT authorship contribution statement

Jungang Zhao: Data curation, Formal analysis, Methodology, Visualization, Writing – original draft. **Qi Yu**: Data curation, Methodology. **Youcai Zhu**: Data curation, Methodology. **Xuan Liu**: Data curation, Methodology. **Shanhong Li**: Data curation, Methodology. **Caixia Liang**: Writing – review & editing. **Ying Zhang**: Writing – review & editing. **Le Huang**: Writing – review & editing. **Kuang Yang**: Writing – review & editing. **Ziang Zhang**: Writing – review & editing. **Yunbo Zhai**: Writing – review & editing. **Caiting Li**: Conceptualization, Funding acquisition, Supervision, Writing – review & editing.

Declaration of Competing Interest

The authors declare that they have no known competing financial interests or personal relationships that could have appeared to influence the work reported in this paper.

Data Availability

Data will be made available on request.

Acknowledgements

This work was financially supported by National Natural Science Foundation of China (52270102) and Natural Science Foundation of Hunan Province (2022JJ40071).

Appendix A. Supporting information

Supplementary data associated with this article can be found in the online version at doi:10.1016/j.jhazmat.2023.131249.

References

[1] Boyjoo, Y., Sun, H., Liu, J., Pareek, V.K., Wang, S., 2017. A review on photocatalysis for air treatment: from catalyst development to reactor design. Chem Eng J 310, 537–559. https://doi.org/10.1016/j.cej.2016.06.090.

[2] Cai, M., Wang, C., Liu, Y., Yan, R., Li, S., 2022. Boosted photocatalytic antibiotic degradation performance of Cd0. 5Zn0. 5S/carbon dots/Bi2WO6 S-scheme heterojunction with carbon dots as the electron bridge. Sep Purif Technol 300, 121892. https://doi.org/10.1016/j.seppur.2022.121892.

[3] Cai, M., Liu, Y., Dong, K., Wang, C., Li, S., 2023. A novel S-scheme heterojunction of Cd0. 5Zn0. 5S/BiOCl with oxygen defects for antibiotic norfloxacin photodegradation: performance, mechanism, and intermediates toxicity evaluation. J Colloid Interface Sci 629, 276–286. https://doi.org/10.1016/j.jcis.2022.08.136.

[4] Cai, M., Liu, Y., Wang, C., Lin, W., Li, S., 2023. Novel Cd0. 5Zn0. 5S/Bi2MoO6 S-scheme heterojunction for boosting the photodegradation of antibiotic enrofloxacin: Degradation pathway, mechanism and toxicity assessment. Sep Purif Technol 304, 122401. https://doi.org/10.1016/j.seppur.2022.122401.

[5] Chang, T., Shen, Z., Huang, Y., Lu, J., Ren, D., Sun, J., Cao, J., Liu, H., 2018. Post-plasma-catalytic removal of toluene using MnO2–Co3O4 catalysts and their synergistic mechanism. Chem Eng J 348, 15–25. https://doi.org/10.1016/j.cej.2018.04.186.

[6] Chen, L., Cui, W., Li, J., Wang, H., Chen, P., Zhou, Y., Dong, F., 2020. The high selectivity for benzoic acid formation on Ca2Sb2O7 enables efficient and stable toluene mineralization. Appl Catal B: Environ 271, 118948. https://doi.org/10.1016/j.apcatb.2020.118948.

[7] Chen, X., Cai, S., Yu, E., Li, J., Chen, J., Jia, H., 2019. Photothermocatalytic performance of ACo2O4 type spinel with light-enhanced mobilizable active oxygen species for toluene oxidation. Appl Surf Sci 484, 479–488. https://doi.org/10.1016/j.apsusc.2019.04.093.

[8] Cui, W., Wang, H., Li, J., Sun, Y., Wang, H., Zhang, Y., Huang, H., Dong, F., 2019. Promoting ring-opening efficiency for suppressing toxic intermediates during photocatalytic toluene degradation via surface oxygen vacancies. Sci Bull 64, 669–678. https://doi.org/10.1016/j.scib.2019.04.020.

[9] Dietzel, P.D.C., Kremer, R.K., Jansen, M., 2004. Tetraorganylammonium superoxide compounds: close to unperturbed superoxide ions in the solid state. J Am Chem Soc 126, 4689–4696. https://doi.org/10.1021/ja039880i.

[10] Dong, C., Qu, Z., Qin, Y., Fu, Q., Sun, H., Duan, X., 2019. Revealing the highly catalytic performance of spinel CoMn2O4 for toluene oxidation: involvement and replenishment of oxygen species using in situ designed-TP techniques. ACS Catal 9, 6698–6710. https://doi.org/10.1021/acscatal.9b01324.

[11] Dong, X. a, Cui, W., Wang, H., Li, J., Sun, Y., Wang, H., Zhang, Y., Huang, H., Dong, F., 2019. Promoting ring-opening efficiency for suppressing toxic intermediates during photocatalytic toluene degradation via surface oxygen vacancies. Sci Bull 64, 669–678. https://doi.org/10.1016/j.scib.2019.04.020.

[12] Duan, J., Song, X., Zhao, H., Zhang, Z., Wang, W., 2020. Self-assembled flower-like (BiO) 2CO3–CdS–CuS stable heterojunction degrades toluene under visible light response. Opt Mater 101, 109761. https://doi.org/10.1016/j.optmat.2020.109761.

[13] Fang, B., Xing, Z., Kong, W., Li, Z., Zhou, W., 2022. Electron spin polarization-mediated charge separation in Pd/CoP@ CoNiP superstructures toward optimized photocatalytic performance. Nano Energy 101, 107616. https://doi.org/10.1016/j.nanoen.2022.107616.

[14] Franchini, C., Podloucky, R., Paier, J., Marsman, M., Kresse, G., 2007. Ground-state properties of multivalent manganese oxides: density functional and hybrid density functional calculations. Phys Rev B 75, 195128. https://doi.org/10.1103/PhysRevB.75.195128.

[15] Gao, F., Chu, C., Zhu, W., Tang, X., Yi, H., Zhang, R., 2019. High-efficiency catalytic oxidation of nitric oxide over spherical Mn Co spinel catalyst at low temperature. Appl Surf Sci 479, 548–556. https://doi.org/10.1016/j.apsusc.2019.02.116.

[16] Gao, M., Teng, W., Du, Z., Nie, L., An, X., Liu, W., Sun, X., Shen, Z., Shi, A., 2021. Source profiles and emission factors of VOCs from solvent-based architectural coatings and their contributions to ozone and secondary organic aerosol formation in China. Chemosphere 275, 129815. https://doi.org/10.1016/j.chemosphere.2021.129815.

[17] Han, D., Gao, S., Fu, Q., Cheng, J., Chen, X., Xu, H., Liang, S., Zhou, Y., Ma, Y., 2018. Do volatile organic compounds (VOCs) emitted from petrochemical industries affect regional PM2. 5? Atmos Res 209, 123–130. https://doi.org/10.1016/j.atmosres.2018.04.002.

[18] Hayyan, M., Hashim, M.A., AlNashef, I.M., 2016. Superoxide ion: generation and chemical implications. Chem Rev 116, 3029–3085. https://doi.org/10.1021/acs.chemrev.5b00407.

[19] Jafari, A.J., Kermani, M., Hosseini-Bandegharaei, A., Rastegar, A., Gholami, M., Alahabadi, A., Farzi, G., 2019. Synthesis and characterization of Ag/TiO2/composite aerogel for enhanced adsorption and photo-catalytic degradation of toluene from the gas phase. Chem Eng Res Des 150, 1–13. https://doi.org/10.1016/j.cherd.2019.07.017.

[20] Ji, F., Men, Y., Wang, J., Sun, Y., Wang, Z., Zhao, B., Tao, X., Xu, G., 2019. Promoting diesel soot combustion efficiency by tailoring the shapes and crystal facets of nanoscale Mn3O4. Appl Catal, B 242, 227–237. https://doi.org/10.1016/j.apcatb.2018.09.092.

[21] Jin, Z., Zhang, Y., Liu, D., Ding, H., Mamba, B.B., Kuvarega, A.T., Gui, J., 2021. Fabrication of a La-doped BiVO4@ CN step-scheme heterojunction for effective tetracycline degradation with dual-enhanced molecular oxygen activation. Sep Purif Technol 277, 119224. https://doi.org/10.1016/j.seppur.2021.119224.

[22] Kong, D., Fan, H., Yin, D., Zhang, D., Pu, X., Yao, S., Su, C., 2021. AgFeO2 nanoparticle/ZnIn2S4 microsphere p–n heterojunctions with hierarchical nanostructures for efficient visible-light-driven H2 evolution. ACS Sustain Chem Eng 9, 2673–2683. https://doi.org/10.1021/acssuschemeng.0c07638.

[23] Kong, J., Xiang, Z., Li, G., An, T., 2020. Introduce oxygen vacancies into CeO2 catalyst for enhanced coke resistance during photothermocatalytic oxidation of typical VOCs. Appl Catal B 269, 118755. https://doi.org/10.1016/j.apcatb.2020.118755.

[24] Lan, L., Shi, Z., Zhang, Q., Li, Y., Yang, Y., Wu, S., Zhao, X., 2018. Defects lead to a massive enhancement in the UV-Vis-IR driven thermocatalytic activity of Co3O4 mesoporous nanorods. J Mater Chem A 6, 7194–7205. https://doi.org/10.1039/c8ta01362d.

[25] Li, A., Zhang, Q., Zhao, S., Chong, Y., Wu, P., Li, Y., Jin, X., Chen, G., Qiu, Y., Yang, S., 2022. A dual plasmonic core—shell Pt/[TiN@ TiO2] catalyst for enhanced photothermal synergistic catalytic activity of VOCs abatement. Nano Res 15, 7071–7080. https://doi.org/10.1007/s12274-022-4380-9.

[26] Li, J.-J., Yu, E.-Q., Cai, S.-C., Chen, X., Chen, J., Jia, H.-P., Xu, Y.-J., 2019. Noble metal free, CeO2/LaMnO3 hybrid achieving efficient photo-thermal catalytic decomposition of volatile organic compounds under IR light. Appl Catal, B 240, 141–152. https://doi.org/10.1016/j.apcatb.2018.08.069.

[27] Li, J.-J., Cai, S.-C., Yu, E.-Q., Weng, B., Chen, X., Chen, J., Jia, H.-P., Xu, Y.-J., 2018. Efficient infrared light promoted degradation of volatile organic compounds over photo-thermal responsive Pt-rGO-TiO2 composites. Appl Catal, B 233, 260–271. https://doi.org/10.1016/j.apcatb.2018.04.011.

[28] Li, K., Jacob, D.J., Liao, H., Zhu, J., Shah, V., Shen, L., Bates, K.H., Zhang, Q., Zhai, S., 2019. A two-pollutant strategy for improving ozone and particulate air quality in China. Nat Geosci 12, 906–910. https://doi.org/10.1038/s41561-019-0464-x.

[29] Li, N., Zhang, J., Tian, Y., Zhao, J., Zhang, J., Zuo, W., 2017. Precisely controlled fabrication of magnetic 3D γ-Fe2O3@ ZnO core-shell photocatalyst with enhanced activity: ciprofloxacin degradation and mechanism insight. Chem Eng J 308, 377–385. https://doi.org/10.1016/j.cej.2016.09.093.

[30] Li, P., Liu, L., An, W., Wang, H., Guo, H., Liang, Y., Cui, W., 2020. Ultrathin porous g-C3N4 nanosheets modified with AuCu alloy nanoparticles and C-C coupling photothermal catalytic reduction of CO$_2$ to ethanol. Appl Catal, B 266. https://doi.org/10.1016/j.apcatb.2020.118618.

[31] Li, Q., Luo, N., Xia, D., Huang, P., Liu, X., Odoom-Wubah, T., Huang, J., Chai, G., Sun, D., Li, Q., 2022. Interfacial effects in CuO/Co3O4 heterostructures enhance benzene catalytic oxidation performance. Environ Sci Nano 9, 781–796. https://doi.org/10.1039/d1en01044a.

[32] Li, S., Dang, X., Yu, X., Abbas, G., Zhang, Q., Cao, L., 2020. The application of dielectric barrier discharge non -thermal plasma in VOCs abatement: a review. Chem Eng J 388. https://doi.org/10.1016/j.cej.2020.124275.

[33] Li, S., Wang, C., Cai, M., Liu, Y., Dong, K., Zhang, J., 2022. Designing oxygen vacancy mediated bismuth molybdate (Bi2MoO6)/N-rich carbon nitride (C3N5) S-scheme heterojunctions for boosted photocatalytic removal of tetracycline antibiotic and Cr (VI): Intermediate toxicity and mechanism insight. J Colloid Interface Sci 624, 219–232. https://doi.org/10.1016/j.jcis.2022.05.151.

[34] Li, S., Cai, M., Liu, Y., Wang, C., Lv, K., Chen, X., 2022. S-Scheme photocatalyst TaON/Bi2WO6 nanofibers with oxygen vacancies for efficient abatement of antibiotics and Cr (VI): Intermediate eco-toxicity analysis and mechanistic insights. Chin J Catal 43, 2652–2664. https://doi.org/10.1016/S1872-2067(22)64106-8.

[35] Li, S., Wang, C., Liu, Y., Liu, Y., Cai, M., Zhao, W., Duan, X., 2023. S-scheme MIL-101 (Fe) octahedrons modified Bi2WO6 microspheres for photocatalytic decontamination of Cr (VI) and tetracycline hydrochloride: synergistic insights, reaction pathways, and toxicity analysis. Chem Eng J 455, 140943. https://doi.org/10.1016/j.cej.2022.140943.

[36] Li, T., Tan, L., Zhao, Y., Song, Y.-F., 2021. Solar-driven hydrogen production from steam methane reforming using highly dispersed metallic Ni catalysts supported on layered double hydroxide nanosheets. Chem Eng Sci 245, 116839. https://doi.org/10.1016/j.ces.2021.116839.

[37] Li, Y., Wu, S., Wu, J., Hu, Q., Zhou, C., 2020. Photothermocatalysis for efficient abatement of CO and VOCs. J Mater Chem A 8, 8171–8194. https://doi.org/10.1039/d0ta00029a.

[38] Li, Y., Wang, L., Zhang, F., Zhang, W., Shao, G., Zhang, P., 2022. Detecting and quantifying wavelength-dependent electrons transfer in heterostructure catalyst via in situ irradiation XPS. Adv Sci 2205020. https://doi.org/10.1002/advs.202205020.

[39] Li, Y., Chen, T., Zhao, S., Wu, P., Chong, Y., Li, A., Zhao, Y., Chen, G., Jin, X., Qiu, Y., 2022. Engineering cobalt oxide with coexisting cobalt defects and oxygen vacancies for enhanced catalytic oxidation of toluene. ACS Catal 12, 4906–4917. https://doi.org/10.1021/acscatal.2c00296.

[40] Li, Z., Li, H., Wang, S., Yang, F., Zhou, W., 2022. Mesoporous black TiO2/MoS2/Cu2S hierarchical tandem heterojunctions toward optimized photothermal-photocatalytic fuel production. Chem Eng J 427, 131830. https://doi.org/10.1016/j.cej.2021.131830.

[41] Liang, C., Li, C., Zhu, Y., Du, X., Zeng, Y., Zhou, Y., Zhao, J., Li, S., Liu, X., Yu, Q., 2022. Light-driven photothermal catalysis for degradation of toluene on CuO/TiO2 composite: dominating photocatalysis and auxiliary thermalcatalysis. Appl Surf Sci 601, 154144. https://doi.org/10.1016/j.apsusc.2022.154144.

[42] Luo, Y., Zheng, Y., Zuo, J., Feng, X., Wang, X., Zhang, T., Zhang, K., Jiang, L., 2018. Insights into the high performance of Mn-Co oxides derived from metal-organic frameworks for total toluene oxidation. J Hazard Mater 349, 119–127. https://doi.org/10.1016/j.jhazmat.2018.01.053.

[43] Luo, Y., Zheng, Y., Feng, X., Lin, D., Qian, Q., Wang, X., Zhang, Y., Chen, Q., Zhang, X., 2020. Controllable P doping of the LaCoO3 catalyst for efficient propane oxidation: optimized surface Co distribution and enhanced oxygen vacancies. ACS Appl Mater Interfaces 12, 23789–23799. https://doi.org/10.1021/acsami.0c01599.

[44] Ma, X., Yang, L., Wu, H., 2021. Removal of volatile organic compounds from the coal-fired flue gas by adsorption on activated carbon. J Clean Prod 302, 126925. https://doi.org/10.1016/j.jclepro.2021.126925.

[45] Ma, Y., Wang, L., Ma, J., Wang, H., Zhang, C., Deng, H., He, H., 2021. Investigation into the enhanced catalytic oxidation of o-Xylene over MOF-derived Co3O4 with different shapes: the role of surface twofold-coordinate lattice oxygen (O2f). ACS Catal 11, 6614–6625. https://doi.org/10.1021/acscatal.1c01116.

[46] Mahmood, A., Shi, G., Xie, X., Sun, J., 2020. Assessing the adsorption and photocatalytic activity of TiO2 nanoparticles for the gas phase acetaldehyde: a computational and experimental study. J Alloy Compd 819, 153055. https://doi.org/10.1016/j.jallcom.2019.153055.

[47] Meng, D., Xu, Q., Jiao, Y., Guo, Y., Guo, Y., Wang, L., Lu, G., Zhan, W., 2018. Spinel structured CoaMnbOx mixed oxide catalyst for the selective catalytic reduction of NOx with NH3. Appl Catal, B 221, 652–663. https://doi.org/10.1016/j.apcatb.2017.09.034.

[48] Meng, X., Wang, T., Liu, L., Ouyang, S., Li, P., Hu, H., Kako, T., Iwai, H., Tanaka, A., Ye, J., 2014. Photothermal conversion of CO(2) into CH(4) with H(2) over Group VIII nanocatalysts: an alternative approach for solar fuel production. Angew Chem Int Ed Engl 53, 11478–11482. https://doi.org/10.1002/anie.201404953.

[49] Mo, S., Zhang, Q., Li, J., Sun, Y., Ren, Q., Zou, S., Zhang, Q., Lu, J., Fu, M., Mo, D., 2020. Highly efficient mesoporous MnO2 catalysts for the total toluene oxidation: oxygen-vacancy defect engineering and involved intermediates using in situ DRIFTS. Appl Catal, B 264, 118464. https://doi.org/10.1016/j.apcatb.2019.118464.

[50] Peluso, M.A., Gambaro, L.A., Pronsato, E., Gazzoli, D., Thomas, H.J., Sambeth, J.E., 2008. Synthesis and catalytic activity of manganese dioxide (type OMS-2) for the abatement of oxygenated VOCs. Catal Today 133–135, 487–492. https://doi.org/10.1016/j.cattod.2007.12.132.

[51] Saqlain, S., Cha, B.J., Kim, S.Y., Ahn, T.K., Park, C., Oh, J.-M., Jeong, E.C., Seo, H. O., Kim, Y.D., 2020. Visible light-responsive Fe-loaded TiO2 photocatalysts for total oxidation of acetaldehyde: fundamental studies towards large-scale production and applications. Appl Surf Sci 505, 144160. https://doi.org/10.1016/j.apsusc.2019.144160.

[52] Shen, Y., Deng, J., Impeng, S., Li, S., Yan, T., Zhang, J., Shi, L., Zhang, D., 2020. Boosting toluene combustion by engineering Co-O strength in cobalt oxide catalysts. Environ Sci Technol 54, 10342–10350. https://doi.org/10.1021/acs.est.0c02680.

[53] Sihaib, Z., Puleo, F., Garcia-Vargas, J.M., Retailleau, L., Descorme, C., Liotta, L.F., Valverde, J.L., Gil, S., Giroir-Fendler, A., 2017. Manganese oxide-based catalysts for toluene oxidation. Appl Catal, B 209, 689–700. https://doi.org/10.1016/j.apcatb.2017.03.042.

[54] Simayi, M., Shi, Y., Xi, Z., Ren, J., Hini, G., Xie, S., 2022. Emission trends of industrial VOCs in China since the clean air action and future reduction perspectives. Sci Total Environ 826, 153994. https://doi.org/10.1016/j.scitotenv.2022.153994.

[55] Solsona, B., Davies, T.E., Garcia, T., Vázquez, I., Dejoz, A., Taylor, S.H., 2008. Total oxidation of propane using nanocrystalline cobalt oxide and supported cobalt oxide catalysts. Appl Catal B: Environ 84, 176–184. https://doi.org/10.1016/j.apcatb.2008.03.021.

[56] Sun, B., Zhou, W., Li, H., Ren, L., Qiao, P., Li, W., Fu, H., 2018. Synthesis of particulate hierarchical tandem heterojunctions toward optimized photocatalytic hydrogen production. Adv Mater 30, 1804282. https://doi.org/10.1002/adma.201804282.

[57] Wang, C., Yan, R., Cai, M., Liu, Y., Li, S., 2023. A novel organic/inorganic S-scheme heterostructure of TCPP/Bi12O17Cl2 for boosting photodegradation of tetracycline hydrochloride: kinetic, degradation mechanism, and toxic assessment. Appl Surf Sci 610, 155346. https://doi.org/10.1016/j.apsusc.2022.155346.

[58] Wang, J., Zhang, G., Zhang, P., 2018. Graphene-assisted photothermal effect on promoting catalytic activity of layered MnO2 for gaseous formaldehyde oxidation. Appl Catal, B 239, 77–85. https://doi.org/10.1016/j.apcatb.2018.08.008.

[59] Wang, J., Gao, X., Wang, Y., Wang, S., Xie, Z., Yang, B., Zhang, Z., Yang, Z., Kang, L., Yao, W., 2022. Multifunctional core-double-shell C@MnO@TiO2 catalysts with enhanced full-light conversion for the highly efficient photothermal oxidation of toluene. Appl Catal, B 317, 121789. https://doi.org/10.1016/j.apcatb.2022.121789.

[60] Wang, L., Li, Y., Wu, C., Li, X., Shao, G., Zhang, P., 2022. Tracking charge transfer pathways in SrTiO3/CoP/Mo2C nanofibers for enhanced photocatalytic solar fuel production. Chin J Catal 43, 507–518. https://doi.org/10.1016/S1872-2067(21)63898-6.

[61] Wang, P., Wang, J., An, X., Shi, J., Shangguan, W., Hao, X., Xu, G., Tang, B., Abudula, A., Guan, G., 2021. Generation of abundant defects in Mn-Co mixed oxides by a facile agar-gel method for highly efficient catalysis of total toluene oxidation. Appl Catal, B 282. https://doi.org/10.1016/j.apcatb.2020.119560.

[62] Wang, Y., Liu, M., Wu, C., Gao, J., Li, M., Xing, Z., Li, Z., Zhou, W., 2022. Hollow nanoboxes Cu2–xS@ ZnIn2S4 core-shell S-scheme heterojunction with broad-spectrum response and enhanced photothermal-photocatalytic performance. Small 18, 2202544. https://doi.org/10.1002/smll.202202544.

[63] Wu, P., Dai, S., Chen, G., Zhao, S., Xu, Z., Fu, M., Chen, P., Chen, Q., Jin, X., Qiu, Y., Yang, S., Ye, D., 2020. Interfacial effects in hierarchically porous α-MnO2/Mn3O4 heterostructures promote photocatalytic oxidation activity. Appl Catal B: Environ 268. https://doi.org/10.1016/j.apcatb.2019.118418.

[64] Yang, J., Xiao, W., Chi, X., Lu, X., Hu, S., Wu, Z., Tang, W., Ren, Z., Wang, S., Yu, X., Zhang, L., Rusydi, A., Ding, J., Guo, Y., Gao, P.-X., 2020. Solar-driven efficient methane catalytic oxidation over epitaxial ZnO/La0.8Sr0.2CoO3 heterojunctions. Appl Catal B 265. https://doi.org/10.1016/j.apcatb.2019.118469.

[65] Yang, M., Yuan, H., Wang, H., Hu, P., 2017. Insights into the selective catalytic reduction of NO by NH3 over Mn3O4(110): a DFT study coupled with microkinetic analysis. Sci China: Chem 61, 457–467. https://doi.org/10.1007/s11426-017-9134-0.

[66] Yang, Y., Li, Y., Zhang, Q., Zeng, M., Wu, S., Lan, L., Zhao, X., 2018. Novel photoactivation and solar-light-driven thermocatalysis on epsilon-MnO2 nanosheets lead to highly efficient catalytic abatement of ethyl acetate without acetaldehyde as unfavorable by-product. J Mater Chem A 6, 14195–14206. https://doi.org/10.1039/c8ta04274h.

[67] Yang, Y., Zhao, S., Bi, F., Chen, J., Wang, Y., Cui, L., Xu, J., Zhang, X., 2022. Highly efficient photothermal catalysis of toluene over Co3O4/TiO2 p-n heterojunction: The crucial roles of interface defects and band structure. Appl Catal, B 315, 121550. https://doi.org/10.1016/j.apcatb.2022.121550.

[68] Yao, J., Dong, F., Feng, H., Tang, Z., 2021. Hierarchical MnO x/Co3O4 nanoarrays on Ni foam for catalytic oxidation of volatile organic compounds. ACS Appl Nano Mater 4, 9322–9332. https://doi.org/10.1021/acsanm.1c01799.

[69] Ye, Z., Giraudon, J.M., Nuns, N., Simon, P., De Geyter, N., Morent, R., Lamonier, J. F., 2018. Influence of the preparation method on the activity of copper-manganese oxides for toluene total oxidation. Appl Catal, B 223, 154–166. https://doi.org/10.1016/j.apcatb.2017.06.072.

[70] Yin, R., Chen, J., Mi, J., Liu, H., Yan, T., Shan, L., Lang, J., Li, J., 2022. Breaking the activity–selectivity trade-off for simultaneous catalytic elimination of nitric oxide and chlorobenzene via FeVO4–Fe2O3 interfacial charge transfer. ACS Catal 12, 3797–3806. https://doi.org/10.1021/acscatal.2c00161.

[71] Zasada, F., Piskorz, W., Stelmachowski, P., Kotarba, A., Paul, J.-F., Płociński, T., Kurzydłowski, K.J., Sojka, Z., 2011. Periodic DFT and HR-STEM studies of surface structure and morphology of cobalt spinel nanocrystals. Retrieving 3D shapes from 2D images. J Phys Chem C 115, 6423–6432. https://doi.org/10.1021/jp200581s.

[72] Zhang, H., Zheng, X., Xu, T., Zhang, P., 2021. Atomically dispersed Y or La on birnessite-type MnO2 for the catalytic decomposition of low-concentration toluene at room temperature. ACS Appl Mater Interfaces 13, 17532–17542. https://doi.org/10.1021/acsami.1c01433.

[73] Zhang, J., Lei, Y., Cao, S., Hu, W., Piao, L., Chen, X., 2022. Photocatalytic hydrogen production from seawater under full solar spectrum without sacrificial reagents using TiO2 nanoparticles. Nano Res 15, 2013–2022. https://doi.org/10.1007/s12274-021-3982-y.

[74] Zhang, M., Gao, H., Chen, J., Elimian, E.A., Jia, H., 2022. Calcination engineering of urchin-like CoO -CN catalysts to enhance photothermocatalytic oxidation of toluene via photo-/thermo- coupling effect. Appl Catal, B 307, 121208. https://doi.org/10.1016/j.apcatb.2022.121208.

[75] Zhang, M., Cai, S., Li, J., Elimian, E.A., Chen, J., Jia, H., 2021. Ternary multifunctional catalysts of polymeric carbon nitride coupled with Pt-embedded transition metal oxide to enhance light-driven photothermal catalytic degradation of VOCs. J Hazard Mater 412, 125266. https://doi.org/10.1016/j.jhazmat.2021.125266.

[76] Zhang, P., Li, Y., Zhang, Y., Hou, R., Zhang, X., Xue, C., Wang, S., Zhu, B., Li, N., Shao, G., 2020. Photogenerated electron transfer process in heterojunctions: in situ irradiation XPS. Small Methods 4, 2000214. https://doi.org/10.1002/smtd.202000214.

[77] Zhang, W., Díez-Ramírez, J., Anguita, P., Descorme, C., Valverde, J.L., Giroir-Fendler, A., 2020. Nanocrystalline Co3O4 catalysts for toluene and propane oxidation: Effect of the precipitation agent. Appl Catal, B 273, 118894. https://doi.org/10.1016/j.apcatb.2020.118894.

[78] Zhang, X., Bi, F., Zhu, Z., Yang, Y., Zhao, S., Chen, J., Lv, X., Wang, Y., Xu, J., Liu, N., 2021. The promoting effect of H2O on rod-like MnCeOx derived from MOFs for toluene oxidation: A combined experimental and theoretical investigation. Appl Catal B: Environ 297. https://doi.org/10.1016/j.apcatb.2021.120393.

[79] Zhang, Y., Zhang, X., Silva, S.R.P., Ding, B., Zhang, P., Shao, G., 2022. Lithium–sulfur batteries meet electrospinning: recent advances and the key parameters for high gravimetric and volume energy density. Adv Sci 9, 2103879. https://doi.org/10.1002/advs.202103879.

[80] Zhang, Y., Zhang, P., Zhang, S., Wang, Z., Li, N., Silva, S.R.P., Shao, G., 2021. A flexible metallic TiC nanofiber/vertical graphene 1D/2D heterostructured as active electrocatalyst for advanced Li–S batteries. InfoMat 3, 790–803. https://doi.org/10.1002/inf2.12214.

[81] Zhao, J., Zhao, Z., Li, N., Nan, J., Yu, R., Du, J., 2018. Visible-light-driven photocatalytic degradation of ciprofloxacin by a ternary Mn2O3/Mn3O4/MnO2 valence state heterojunction. Chem Eng J 353, 805–813 https://doi.org/10.016/j.cej.2018.07.1613.

[82] Zhao, J., Guo, X., Shi, R., Waterhouse, G.I.N., Zhang, X., Dai, Q., Zhang, T., 2022. NiFe nanoalloys derived from layered double hydroxides for photothermal synergistic reforming of CH4 with. Adv Funct Mater 2204056, CO2. https://doi.org/10.1002/adfm.202204056.

[83] Zhao, J., Li, C., Du, X., Zhu, Y., Li, S., Liu, X., Liang, C., Yu, Q., Huang, L., Yang, K., 2022. Recent progress of carbon dots for air pollutants detection and photocatalytic removal: synthesis, modifications, and applications. Small 2200744. https://doi.org/10.1002/smll.202200744.

[84] Zhao, Q., Zheng, Y., Song, C., Liu, Q., Ji, N., Ma, D., Lu, X., 2020. Novel monolithic catalysts derived from in-situ decoration of Co3O4 and hierarchical Co3O4@MnOx on Ni foam for VOC oxidation. Appl Catal, B 265, 118552. https://doi.org/10.1016/j.apcatb.2019.118552.

[85] Zhao, Q., Du, Q., Yang, Y., Zhao, Z., Cheng, J., Bi, F., Shi, X., Xu, J., Zhang, X., 2022. Effects of regulator ratio and guest molecule diffusion on VOCs adsorption by defective UiO-67: experimental and theoretical insights. Chem Eng J 433, 134510. https://doi.org/10.1016/j.cej.2022.134510.

[86] Zhao, W., Zhang, Y., Wu, X., Zhan, Y., Wang, X., Au, C.-T., Jiang, L., 2018. Synthesis of Co–Mn oxides with double-shelled nanocages for low-temperature toluene combustion. Catal Sci Technol 8, 4494–4502. https://doi.org/10.1039/c8cy01206g.

[87] Zheng, Y., Wang, W., Jiang, D., Zhang, L., 2016. Amorphous MnOx modified Co3O4 for formaldehyde oxidation: improved low-temperature catalytic and photothermocatalytic activity. Chem Eng J 284, 21–27. https://doi.org/10.1016/j.cej.2015.08.137.

[88] Zheng, Y., Wang, W., Jiang, D., Zhang, L., Li, X., Wang, Z., 2016. Ultrathin mesoporous Co3O4 nanosheets with excellent photo-/thermo-catalytic activity. J Mater Chem A 4, 105–112. https://doi.org/10.1039/c5ta07617j.

[89] Zhong, J., Zeng, Y., Zhang, M., Feng, W., Xiao, D., Wu, J., Chen, P., Fu, M., Ye, D., 2020. Toluene oxidation process and proper mechanism over Co3O4 nanotubes: Investigation through in-situ DRIFTS combined with PTR-TOF-MS and quasi in-situ XPS. Chem Eng J 397, 125375. https://doi.org/10.1016/j.cej.2020.125375.

[90] Zhou, A., Liu, J.-L., Zhu, B., Li, X.-S., Zhu, A.-M., 2022. Plasma catalytic removal of VOCs using cycled storage-discharge (CSD) mode: an assessment methodology based on toluene for reaction kinetics and intermediates. Chem Eng J 433, 134338. https://doi.org/10.1016/j.cej.2021.134338.

[91] Zhu, M., Huang, H., Wang, Y., Huang, Z., Zhang, X., Tang, M., Lu, M., Chen, C., Shi, B., Chen, Z., 2021. A newly integrated dataset of volatile organic compounds (VOCs) source profiles and implications for the future development of VOCs profiles in China. Sci Total Environ 793, 148348. https://doi.org/10.1016/j.scitotenv.2021.148348.

[92] Zuo, G., Wang, Y., Teo, W.L., Xie, A., Guo, Y., Dai, Y., Zhou, W., Jana, D., Xian, Q., Dong, W., 2020. Ultrathin ZnIn2S4 nanosheets anchored on Ti3C2TX MXene for photocatalytic H2 evolution. Angew Chem 132, 11383–11388. https://doi.org/10.1002/ange.202002136.